UNIVERSITY OF CALIFORNIA,
IRVINE

Growth and Characterization of Skyrmion-hosting Magnetic Thin Films

DISSERTATION

submitted in partial satisfaction of the requirements
for the degree of

DOCTOR OF PHILOSOPHY

in Physics

by

Brian J. Youngblood

Thesis Committee:
Professor Ilya N. Krivorotov, Chair
Professor Philip G. Collins
Professor Alexander L. Chernyshev

2015

TABLE OF CONTENTS

LIST OF FIGURES

ACKNOWLEDGMENTS

I would like to express my gratitude to my advisor, Professor Ilya Krivorotov for giving me the opportunity to pursue the line of research presented here as well as always providing clear assessment, guidance, and every resource and example one could ever need to develop as a scientist. I would also like to thank my dissertation committee for helping me to improve this document and my presentation of its content. Funding support from the National Science Foundation also made this work possible and is gratefully acknowledged. I am also thankful to and for my colleagues in the lab: Yu-Jin, Graham, Zheng, Chris, Alejandro, Liu, Jen-Ru, Igor, Andy, Jieyi, Cheng-Cen, and Jian who unstintingly shared their expertise, questions, answers, and ideas with me. I also thank Dr. Qiyin Lin for discussions, training, and assistance as well as Hua Wen and Patrick Odenthal for their help on a different project. Finally, my thanks to my father, who has recognized, shared, and encouraged my curiosity all my life and has always believed in me.

CURRICULUM VITAE

Brian J. Youngblood

Education

University of California Irvine *Physics* Ph.D. 2016

University of California Irvine *Physics* M.Sc. 2012 Thesis: "Wireless Microwave Detection Using Magnetic Tunnel Junctions"

Massachuesetts Institute of Technology *Nuc. Engr.* M.Sc. 2004 Thesis: "Bolometer diagnostics on Alcator C-mod"

University of California San Diego *Physics* B.Sc. 2001 Dept. Honors Thesis: "Levitated coil stability for LDX experiment."

Appointments

Graduate Student Researcher, Dept. of Physics, UC Irvine *2008-2015*

GAANN Fellow, Dept. of Physics, UC Irvine *2007-2010*

Ford Foundation Predoctoral Fellow, Dept. of Nuc. Engr., MIT *2001-2004*

Awards

- AMS Poster Award, SACNAS Conference 2000

- MIT Summer Research Program 2000

- McNair Scholar UCSD 1999

Publications and Presentations

-Brian Youngblood, Ilya N. Krivorotov **Electrical Detection of a Skyrmion State in Sputter Deposited MnSi Thin Films** (*in preparation*)

-Liu Yang, Roman Verba, Vasil Tiberkevich, Tobias Schneider, Andrew Smith, Zheng Duan, Brian Youngblood, Kilian Lenz, Jürgen Lindner, Andrei N. Slavin, and Ilya N. Krivorotov **Reduction of phase noise in nanowire spin orbit torque oscillators** *Nat. Sci. Rep.* 5, 16942

-I. Barsukov, Yu Fu, Y.-J. Chen, B. Youngblood, A.M. Gonçalves, M. Spasova, M. Farle, J.A. Katine, and I.N. Krivorotov, **Magnetic phase transitions in Ta/-CoFeB/MgO multilayers** *Applied Physics Letters* 106, 19247 (2015)

-Zheng Duan*, Andrew Smith*, Liu Yang*, Brian Youngblood*, Jürgen Lindner, Vladislav Demidov, Sergej Demokritov, and Ilya Krivorotov **Nanowire Spin Torque Oscillator Driven by Spin Orbit Torques** *Nat. Comm.* 5, 5616 (2014)(*these authors contributed equally)

-*Brian Youngblood*, **Skyrmions in Thin Films: Properties and a Proposal for Observation by SEMPA**, NIST Center for Nanoscale Science and Technology Electron Physics Group Seminar 4/3/2014 (Oral Presentation)

-*Brian Youngblood*, Ilya N. Krivorotov **Electrical Detection of a Skyrmion State in Sputter Deposited MnSi Thin Films**, APS March Meeting 2014 (Oral Presentation)

-*Brian Youngblood*, Ilya N. Krivorotov **Electrical Detection of a Skyrmion State in Sputter Deposited MnSi Thin Films**, MMM Conference 2013 (Poster Presentation)

-*Brian Youngblood*, Ilya N. Krivorotov **"Spin Hall Effect and Control of Ferromagnetic Electrodes"** (Oral Presentation), NEB Project Meeting Jan. 9, 2013

-*Brian Youngblood*, Ilya N. Krivorotov **Free Layer Switching for Magnetologic Gates** (Poster Presentation), NEB Review Meeting July, 2012

-*Liu Yang*, Andrew Smith, Brian Youngblood, Zheng Duan, Ilya Krivorotov, **Tapered nanowire spin torque oscillator driven by spin orbit torques**, APS March Meeting 2015 (Oral Presentation, paper in preparation)

-*Alejandro Jara*, Igor Barsukov, Brian Youngblood, Brian Youngblood, John Read, Patrick Bragnaca, Ilya Krivorotov, **Epitaxial $IrMn_3$ on MgO(111) by sputter deposition**, APS March Meeting 2015 (Oral Presentation, paper in preparation)

-*Andrew Smith*, Liu Yang, Brian Youngblood, Zheng Duan, Ilya Krivorotov, **Time domain measurements of a spin torque oscillator driven by spin orbit**

torques (Oral Presentation), MMM Conference, Nov. 2014

-*Igor Barsukov*, Yu Fu, Chris Safranski, Yu-Jin Chen, Brian Youngblood, Alexandre M. Gonalves, Luiz C. Sampaio, Marina Spasova, Michael Farle, Ilya Krivorotov, **Field-dependent perpendicular magnetic anisotropy and interfacial metal-insulator transition in CoFeB/MgO systems** (Oral Presentation), MMM Conference, Nov. 2014

-*Liu Yang*, Andrew Smith, Brian Youngblood, Zheng Duan, Ilya Krivorotov, **Tapered nanowire spin torque oscillators driven by spin orbit torques** (Oral Presentation), MMM Conference, Nov. 2014

-*Andrew Smith*, Zheng Duan, Liu Yang, Brian Youngblood, Ilya Krivorotov **Nanowire Spin Torque Oscillator Driven by Spin Orbit Torques**, American Physical Society March Meeting 2014

-*Ilya Krivorotov*, Zheng Duan, Andrew Smith, Liu Yang, Brian Youngblood **Nanowire spin torque oscillator driven by spin orbit torques** (Oral Presentation), KITP Conference: Concepts in Spintronics 2013

-*Jing Zhao*,Brian Youngblood, Ilya Krivorotov, Kang L. Wang **Temperature dependent magnetization reversal and compensation points in ferrimagnetic GdFeCo films** (Oral Presentation), MMM Conference 2013

-*Liu Yang*, Zheng Duan, Andrew Smith, Brian Youngblood, Ilya Krivorotov **Electrical detection of parametric spin wave resonance in permalloy/platinum nanowires** (Oral Presentation) MMM Conference 2013

-*Zheng Duan*, Andrew Smith, Liu Yang, Brian Youngblood, Ilya N. Krivorotov **Nanowire Spin Hall Oscillator** (Oral Presentation) MMM Conference 2013

-David Carlton, Brian Lambson, Zheng Gu, Scott Dhuey, Li Gao, Brian Hughes, Deirdre Olynick, Charles Rettner, Andreas Scholl, Brian Youngblood, Anthony Young, Ilya Krivorotov, Stuart Parkin and Jeffrey Bokor **"Signal propagation in dipole coupled nanomagnets for logic applications"**, *Proc. SPIE* 8461, Spintronics V, 84610W (2012)

ABSTRACT OF THE DISSERTATION

Growth and Characterization of
Skyrmion-hosting Magnetic Thin Films

By

Brian J. Youngblood

Doctor of Philosophy in Physics

University of California, Irvine, 2015

Professor Ilya N. Krivorotov, Chair

Magnetic skyrmions are particle-like knots of magnetization which are both highly stable under the proper conditions and at the same time very easy to move and rotate. These properties make them very promising as a basis for future spin electronic information storage and manipulation. At the same time, these structures exhibit interesting fundamental physics including emergent mass and electrodynamics and phase transitions including a crystalline state as well as being low-dimensional analogues of a model of low-energy sub-atomic particles. Accessibility to studying these objects is hampered by the fact that most skyrmion-hosting materials have to be grown either as single crystals or by molecular beam epitaxy (MBE). Also, predictive studies are currently mostly restricted to full numerical simulations because of the intractability of the equation describing skyrmion structure and a dearth of analytical approximations.

In this dissertation, I present work on the sputter deposition of the skyrmion hosting chiral magnetic material MnSi. MnSi was the first material observed to exhibit a skyrmion state but it has not been made by sputtering until now. I demonstrate by x-ray diffractometry and electrical measurements that the sputter-deposited

MnSi exhibits properties similar to those of MBE-grown thin films including hosting skyrmions. This will hopefully improve the accessibility of experimental studies of MnSi and skyrmions. I also present an approximation for skyrmion spatial profiles which can predict skyrmion structure in a physically interesting range of material parameters and external magnetic fields. Using this structural approximation it should be possible to predict skyrmion stability and behavior under different conditions more rapidly than is possible with numerical simulations.

Chapter 1

Introduction

As consumer devices approach the physical limits of silicon technology in terms of miniaturization and efficient operation [1, 2] there has been strong and steadily growing interest in alternatives to semiconductor-based transistor logic and fast-access storage [3]. Due to the prevalence and continued popularity of mobile devices and the importance of energy conservation, one key feature of any competitive technology will be low energy consumption. Two principal ways of accomplishing this goal are to have memory or logic elements which do not require continuous or rapidly repeated application of power to maintain their state (such elements are often referred to as "non-volatile") and/or elements which require little power to switch from one measureable state to another. A problem arises in that these two characteristics appear at first glance to be antithetical: A low energy barrier for state switching or manipulation typically implies low stability and conversely a system in a stable state almost by definition requires a significant amount of energy to change.

One way around this fundamental problem is to use manipulable, stable objects and describe the state of the system in terms of spatial arrangements of these objects. A

good example of this is the magnetic domain wall "racetrack memory" invented by S.S.P. Parkin [4, 5, 6] and currently pursued by him and other researchers at IBM. In this design, data is stored as the presence or absence of a domain wall in a magnetic nanowire. These domain walls are written and read by current induced spin transfer torques applied to the nanowire via (e.g.) ferromagnetic leads. The whole sequence of domain walls can be moved at high speeds by currents in the nanowire resulting in orders of magnitude faster data access than in current magnetic hard drive storage technology.

The downside of this impressive technology is the relatively high current density required to induce domain wall motion (of order 10^{12} Am^{-2} [5]). This high current density results in undesirably large power consumption and heat dissipation, even in an all metal device, since both increase as the square of the current density. The problem of high current densities plagues many other spintronic technologies such as spin valve and magnetic tunnel junction based ST-MRAM (magnetic random access memory, examples of which are already produced commercially [7]) that share the property of non-volatility (one of their main attractions) with the racetrack memory but require of order 10^{10} Am^{-2} to switch the magnetization direction of their free magnetic layer [8].

A very promising alternative to a magnetic domain wall for the "stable object" discussed above is a magnetic skyrmion [9, 10], a long predicted [11] but only recently realized [12] magnetic structure. Skyrmions are arrangements of electron spins (see Fig. 1.1) which share features with both magnetic vortices and domain walls. They take their name from particle physicist T.H.R. Skyrme who developed a model for hadronic particles in which hadrons were three dimensional skyrmions [13]. In the context of magnetic materials, and in particular thin films, skyrmions are treated as two dimensional structures though some research indicates that they have out of

plane structure in thicker samples [14]. They will be considered 2D objects for the purposes of this thesis.

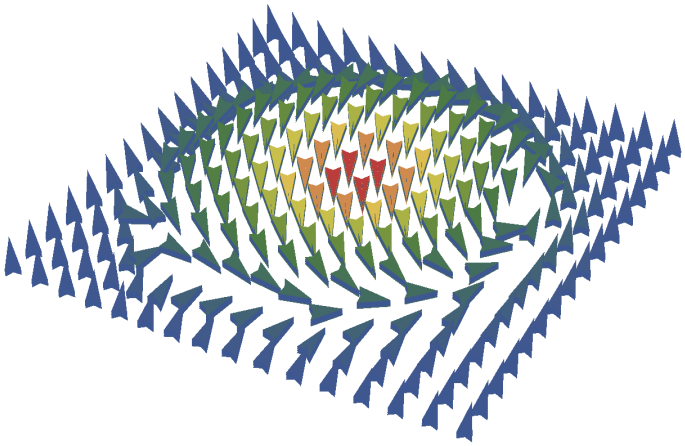

Figure 1.1: A skyrmion spin structure.

Skyrmions are stable in the sense that the skyrmion number given by Eq. (2.1) is an invariant quantity. Skyrmions are therefore essentially indestructible once formed except under direct and specific interactions as long as the general conditions for their stability are maintained and they are not annihilated by an anti-skyrmion (which typically cannot form under the same conditions). This excellent stability is part of what makes skyrmions so promising for information storage and processing applications.

In extended samples, skyrmions are typically observed as elements of skyrmion crystals (see Fig. 1.2) over much of their regime of stability [15]. These skyrmion crystals are quite similar to Abrikosov vortex crystals in type-II superconductors. They possess a similar hexagonal structure and can melt into individual dissociated solitons at the edges of their region of stability. However, unlike vortices, the radial profile of a skyrmion is not singular at the center. As a consequence, skyrmion stability is improved in comparison to vortices in ferromagnets, to which they are also similar, and they are easier to move and less susceptible to pinning by impurities or defects [16]. Skyrmions are also considerably easier to manipulate and move than magnetic

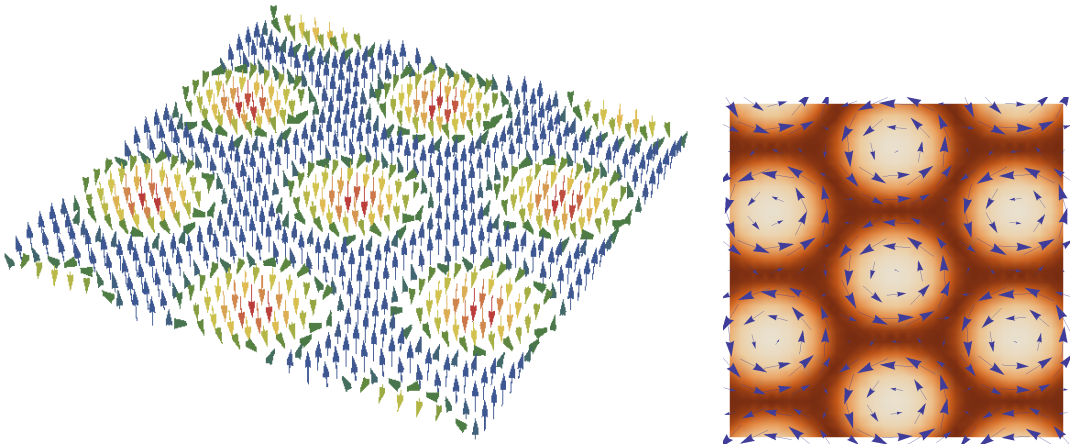

(a) (b)

Figure 1.2: Skyrmion lattice magnetization structure: (a) Angled view showing magnetization structure. (b) Projection with view along the axis perpendicular to the skyrmion crystal plane, color represents the component of magnetization along the viewing axis. The darkest color represents magnetization fully out of the plane of the page and the lightest color represents magnetization fully into the plane.

domain walls of all kinds, requiring only of order 10^5 Am^{-2} to move or rotate in some materials [17].

From a physics standpoint, skyrmions in magnetic materials have many fascinating properties and are accessible analogues to many other important physical systems. Firstly, they are known to exist in sizes ranging from atomic scales to nearly $100nm$, and the long-range (skyrmion crystal) order of the larger ones (>1nm in size), though clearly associated with particular underlying crystal structures, can also apparently be completely decoupled from them [18]. Individual skyrmions are emergent (from a generally well understood background field) particle-like objects, possess an emergent mass [19, 20] and produce emergent effective magnetic and electric fields [21] which are detectable via accessible electrical measurements. Magnetic skyrmion crystals are also predicted [22] to exhibit an analogue of the quantum anomalous Hall effect observed in magnetic topological insulators [23, 24]. Magnetic skyrmions are also analogous to the skyrmions observed in quantum Hall effect systems [25] and some-

what more experimentally accessible. Finally, they are low-dimensional analogues of their original incarnation as low-energy approximations to baryons [13].

Currently, very costly and low through-put single crystal and MBE growth methods are the norm for producing chiral ferromagnets which can host magnetic skyrmions (with the notable exception of FeGe). This limits opportunities for study and makes it impractical, in a commercial sense, to develop information technology systems based on skyrmions. If the full potential applications of skyrmions are to be realized, and their interesting physical properties explored efficiently, then it is necessary to have accessible, lower-cost means of producing skyrmion-hosting materials.

In this thesis, I explore the deposition of the original and prototypical skyrmion-hosting compound MnSi by DC magnetron sputtering at elevated temperatures. First, successful deposition techniques were developed and secondly it was demonstrated by electrical measurements that MnSi thin films produced by sputtering are capable of hosting skyrmions and are in fact comparable to MBE-grown MnSi in this regard.

In addition to the availability of materials, the development of technology based on skyrmions depends on being able to model their behavior under various conditions. At the time of this writing, this is accomplished either by approximating skyrmions as rigid, structureless particles [16] or by carrying out full micromagnetic calculations numerically [26]. This last approach can be challenging and time-consuming because of the relatively large size and complexity of skyrmions and the need to model their behavior in quite large structures if one is to simulate (e.g.) a racetrack structure.

In Chapter 7 I present an approximation for the spatial profile of a skyrmion, demonstrate its consistency with numerical solutions, and then present a means of approximating the energy integral for this structure analytically. The result is a useful analytical approximation that should both capture more of the skyrmion behavior

than the particle model and be quicker and easier to apply than the micromagnetic simulations.

Chapter 2

Skyrmions

2.1 History and General Description

Skyrmions are magnetization structures characterized by a double winding of local spin orientation which are topologically protected, meaning that they cannot be destroyed by continuous, low-energy deformation. This protection is encapsulated in the topologically invariant skyrmion number given by

$$N_{sk} = \frac{1}{4\pi} \int \vec{m} \cdot \left(\frac{\partial \vec{m}}{\partial x} \times \frac{\partial \vec{m}}{\partial y} \right) d\Omega \tag{2.1}$$

where $\vec{m}(\vec{r})$ is the orientation of the magnetization at position $\vec{r}$ and Ω is the solid angle, is a conserved quantity (as well as being quantized due to the particle-like nature of the skyrmions).

As soliton (particle-like in structure and interaction behavior [27, 28]) solutions to nonlinear sigma models [29] in particle physics, skyrmions were introduced by Skyrme [13] as a proposal for the nature and structure of fundamental particles prior to

the development of quantum chromodynamics. The Heisenberg model describing magnetic materials is also one of this type of mathematical model.

These structures first arose in the context of condensed matter physics in the course of studies of the quantum Hall effect [30, 31, 25]. Here the skyrmions are stabilized by the Coulomb interaction and to a lesser extent the Zeeman interaction with the applied magnetic field [32]. The question of whether skyrmions in magnetic materials also possess electric charge as the QHE skyrmions do remains open because while there are theoretical arguments supporting the possibility [33], there is no experimental evidence either way.

In magnetic materials, skyrmions were found to be solutions to a modified Heisenberg model by Belavin and Polyakov [34] with the explicit connection to the earlier particle physics model made by Bogdanov and Hubert [35]. In this model the Skyrme term is contributed by the Dzyaloshinskii-Moriya interaction (DMI), a form of spin-orbit interaction. Recently, among bulk (weak) chiral ferromagnets (a ferromagnet whose crystal structure cannot be superimposed on its mirror image, see Chapter 4), skyrmions have been observed directly and indirectly in all compositions of $Mn_{1-x}Fe_xGe$, most compositions of $Fe_{1-x}Co_xSi$ (including semiconducting ones), and those of $Mn_{1-x}Fe_xSi$ with $x \leq 0.1$, as well as the insulator Cu_2OSeO_3.

In this chapter we will describe the theory of the DMI beginning with spin-orbit interaction in general and following recent developments in this area, culminating in a description of static skyrmions and relying throughout on the concepts of geometric or Berry phase [36, 37, 38] and holonomy [39, 40].

2.2 Spin-Orbit Interaction

The spin-orbit coupling in condensed matter systems arises because the spin angular momentum of an electron $\vec{S} = \pm\frac{1}{2}\hbar$ [41] in a material interacts with the (orbital) angular momentum $\vec{L} = m_e\vec{r} \times \vec{v}$ resulting from the electron's motion in response to the background fields it experiences in the material at position $\vec{r}$ as it moves with velocity $\vec{v}$. This begs the question of why the two angular momenta (intrinsic and extrinsic) should interact.

In the simplest case, we can think in terms of the Bohr picture where the electron is "orbiting" the nucleus of a hydrogen-like atom and is affected by that orbital motion. For this model we follow the derivation by Jackson [42]. Lorentz transformation of electromagentic fields gives (to first order) a total magnetic field experienced by the electron (in its rest frame) of

$$\vec{B}' \approx \vec{B} - \frac{\vec{v}}{c} \times \vec{E} \tag{2.2}$$

We take the externally applied magnetic field $\vec{B}$ to be 0 and the electric field $\vec{E}$ experienced by the electron to be entirely due to the charge of the nucleus (for a hydrogen atom) and so written as $\vec{E} = \frac{-1}{e}\nabla V(r)$ where $V(r)$ is a spherically symmetric electric potential. The presence of the second term in Eq. (2.2) means that the electron's magnetic moment $\vec{\mu} = \frac{ge}{m_e c}\vec{s}$ experiences a torque (as observed in its rest frame)

$$\frac{d\vec{s}}{dt} = \vec{\mu} \times \left(-\frac{\vec{v}}{c} \times \frac{-1}{e}\frac{\vec{r}}{r}\frac{dV}{dr} \right) \tag{2.3}$$

Which can be rewritten as

$$\frac{d\vec{s}}{dt} = \frac{g}{2m^2c^2}\vec{s} \times \vec{L}\frac{1}{r}\frac{dV}{dr} \tag{2.4}$$

The corresponding interaction energy is

$$E_{SOI} = \frac{g}{2m^2c^2}\vec{s}\cdot\vec{L}\frac{1}{r}\frac{dV}{dr} \tag{2.5}$$

This already demonstrates an interaction between spin and orbital angular momentum but the derivation is incomplete, and the magnitude of this spin-orbit expression disagrees with experimental results. It was pointed out by Thomas [43] that since the electron's rest frame is in fact traveling in a circular path about the nucleus (in the laboratory and nucleus' rest frame), and therefore accelerating (and so not in an inertial frame) the electron spin precesses and there is an additional spin-orbit term produced [42] so that

$$\frac{d\vec{s}}{dt} = \frac{g}{2m^2c^2}\vec{s}\times\vec{L}\frac{1}{r}\frac{dV}{dr} + \omega_T\times\vec{s} \tag{2.6}$$

This is a purely kinematic result, even nonrelativistic objects observed from a rotating frame of reference have such an additional component in their motion (e.g. Coriolis effect [44]).

In this situation the additional term arises because the circular motion of the electron can be thought of as being made up of a sequence of *noncollinear* Lorentz boosts. A sum of two such boosts is equivalent to a single boost plus a rotation [45, 46]. If we consider the instantaneous laboratory-frame velocity of the electron to be $\vec{v}+\vec{a}dt$ (where $\vec{a}$ is the electron's acceleration) rather than just $\vec{v}$ as we have been so far, then we have exactly this situation and each infinitesimal time step dt will contribute a rotation of the electron spin vector $\vec{s}$ by

$$\Delta\vec{s} = \frac{\gamma^2}{\gamma+1}\frac{1}{c^2}\vec{a}\times\vec{v}dt\times\vec{s} \tag{2.7}$$

and for $v \ll c$ this gives $\vec{\omega}_T = \frac{1}{2c^2}\vec{a}\times\vec{v}$. This rotation is the Thomas precession of the

spin. Since $\vec{a}$ comes from the electrical force due to the nucleus $\frac{1}{m}\frac{\vec{r}}{r}V(r)$ the correction to the energy of Eq. (2.5) is

$$\Delta E_T = \frac{-1}{2m^2c^2}\vec{s}\cdot\vec{L}\frac{1}{r}\frac{dV}{dr} \tag{2.8}$$

Allowing the correct and experimentally confirmed spin-orbit interaction energy to be obtained.

Ultimately, this term arises because the Lorentz transformation is not commutative under direction changes and Thomas's precessional term is a measure of that non-commutativity. This was shown by Wigner [46]. This fact connects the Thomas precession to the concept of holonomy which can be thought of as the measure of non-commutativity of a transformation. This in turn connects to other examples of holonomy which go under the heading of geometric phase.

The background field acting on the electron need not be the simple, spherically symmetric field due to a single nucleus. In materials the field experienced by the moving electron is often best described by the electronic band structure of the material. As we will see in the following sections, in all cases relevant to this thesis, it can be shown that spin-orbit interaction is *itself* a geometric phase effect.

2.3 Geometric Phase

2.3.1 Classical

A classical, real space example of a geometric phase effect can be seen in the parallel transport of a vector along a closed path on the surface of a sphere (Fig. 2.1). The idea of parallel transport is that the vector remains constant in the sense that its

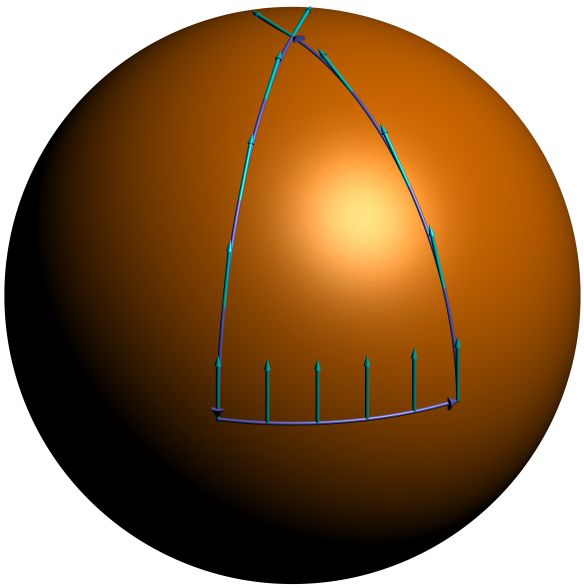

Figure 2.1: A vector parallel transported (counter-clockwise) along a closed path on the surface of a sphere. The path begins and ends at the north pole, where the angle between the vector at the start and at the end of its travel can be seen.

local orientation with respect to the surface of the sphere never changes. When the vector returns to its starting point it is rotated with respect to its initial absolute orientation by an angle equal to the solid angle enclosed by the path traveled, which for a sphere is also the total curvature enclosed. This change in angle is a geometric phase.

The acquisition of a geometric phase angle is not restricted to motion on spherical surfaces, but only requires a curved surface. The magnitude of the change in angle is the amount of "bending" of the path:

$$\Delta\alpha = \frac{S}{R^2} = \oint_C \vec{A} \cdot d\vec{l} \tag{2.9}$$

where S is the area enclosed and R is the radius of curvature. This is equivalent (via

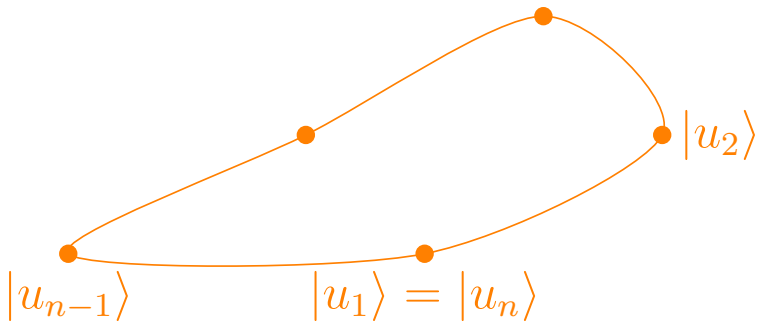

Figure 2.2: A closed path in an abstract state space with an adiabatic parameter indicated by subscripts.

Stokes' theorem) to the total curvature enclosed by the path:

$$\Delta\alpha = \int_S d\vec{S} \cdot (\vec{\nabla} \times \vec{A}) = \int_S d\vec{S} \cdot \vec{\Omega} \tag{2.10}$$

In these expressions $\vec{A}$ is a vector field which in this case represents the orientation of the unit vector normal to the sphere's surface.

2.3.2 Quantum Geometric Phase

When studying the quantum dynamics of electrons the analogous phase angle is often referred to as Berry's phase after M.V. Berry who first realized its physical significance in this context [36]. Here it is important to consider the adiabatic evolution of the system being studied as it traverses a closed path (Fig. 2.2) in momentum space (Fig. 2.3). The adiabatic theorem [36] requires that for a sufficiently slow evolution the system remains in the same eigenstate and over the complete closed path is only modified by a phase $\Delta\alpha$ so that:

$$|u_n\rangle = e^{i\Delta\alpha} |u_1\rangle \tag{2.11}$$

The full phase is just the sum of the individual phase changes corresponding to each step of the closed-cycle evolution of the system:

$$\Delta\alpha = i\left(ln[\langle u_1|u_2\rangle\,\langle u_2|u_3\rangle\,...\,\langle u_{n-1}|u_n\rangle]\right) \tag{2.12}$$

Since the eigenstate remains unchanged, we can make the path continuous by making the momentum space separation between adjacent steps of the system's evolution infinitesimally small so that:

$$\Delta\alpha = i\oint dk\,\langle u_k|\partial_k u_k\rangle \tag{2.13}$$

We can also write this integration over adiabatic changes in momentum space as:

$$\Delta\alpha = i\oint d\vec{k}\cdot\langle\vec{k}|\,\nabla_k\,|\vec{k}\rangle \tag{2.14}$$

The integrand in Eq. (2.14) is a vector potential often referred to as the Berry connection

$$\vec{A} = \langle\vec{k}|\,i\nabla_k\,|\vec{k}\rangle \tag{2.15}$$

The elements of this vector potential are the overlap integrals of two wave functions at infinitesimally separated points in k-space.

As in the classical version above, Stokes' theorem lets us rewrite Eq. (2.14) as a surface integral of the (Berry) curvature $\Omega(\vec{k}) = \nabla\times\vec{A}$.

$$\Delta\alpha = \int\int_S \Omega_z(\vec{k})d^2\vec{k} = \int\int_S i\,\langle\frac{du}{dk_x}|\times|\frac{du}{dk_y}\rangle\,d^2\vec{k} \tag{2.16}$$

This is the total curvature, but in quantized momentum space rather than real space. For concreteness it is useful to think of u as the wave functions of Bloch electrons

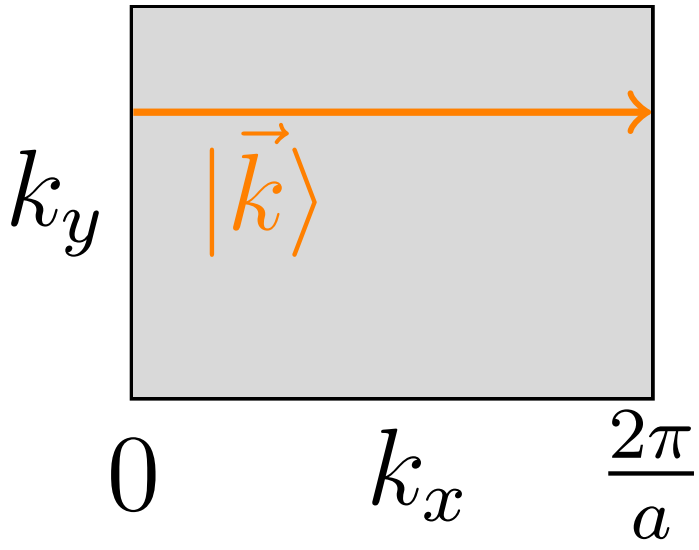

Figure 2.3: A path in a Brillouin zone, it is closed because the left and right edges are identified with each other.

in a crystal (especially since this is the case that will be important for the transport measurements in this thesis) so that the appropriate region of integration is a Brillouin zone (BZ) (Fig. 2.3), assuming that the path in momentum space bounds the entire BZ, which Bloch electrons typically will because their wave functions have a component periodic in k and the BZ has the topology of a flat torus (edges identified with each other) [47, 48]. To get the total Berry phase the integral over the Brillouin zone also has to be summed over the occupied states n, all of which contribute. The momentum space distribution of the electrons is also important (see below).

In order to obtain the $\partial_{k_i} |u_{nk}\rangle$ we begin by working in a gauge such that the local Berry connection is zero ($\langle\vec{k}| \nabla_k |\vec{k}\rangle = 0$) on some small portion of a closed path in k-space. It should be stressed that this can never be the case over any whole closed path because the total Berry phase (Eq. (2.13)) is gauge invariant. This is akin to the classical case on the sphere discussed above where it was possible for the vector to remain unchanged relative to the surface in a local sense while still acquiring a finite absolute rotation with respect to its initial orientation. Within this gauge we

can take a set of starting $|u_{n\tilde{k}}\rangle$ at an arbitrarily chosen starting momentum $\tilde{k}$ and form the basis states for an infinitesimally nearby $\tilde{k}+\epsilon$ using perturbation theory [49]

$$|u_{n,k+\epsilon}\rangle = |u_{nk}\rangle + \sum_{m\neq n} \frac{\langle u_{nk}| H(k+\epsilon) - H(k) |u_{mk}\rangle}{(E_{nk} - E_{mk})} |u_{mk}\rangle \tag{2.17}$$

Where for this section $H(\vec{k})$ is the Hamiltonian of the system, satisfying $H(k)|u_{nk}\rangle = E_{nk}|u_{nk}\rangle$. If we then subtract $|u_{nk}\rangle$ from both sides, divide by ϵ and take the limit as $\epsilon 0$ we have defined the derivative of $|u_{nk}\rangle$ with respect to k (or a component thereof) along a path. So the derivatives on the right hand side of Eq. (2.16) can now be written as

$$\partial_{k_i} |u_{nk}\rangle = \sum_{m\neq n} \frac{\langle u_{nk}| \partial_{k_i} H |u_{mk}\rangle}{(E_{nk} - E_{mk})} |u_{mk}\rangle \tag{2.18}$$

And the components of the curvature tensor (for the n-th band) are now given by

$$\Omega^n_{ij}(\vec{k}) = 2i \sum_{m\neq n} \frac{\langle u_{nk}| \partial_{k_i} H |u_{mk}\rangle \langle u_{mk}| \partial_{k_j} H |u_{nk}\rangle}{(E_{mk} - E_{nk})^2} \tag{2.19}$$

The denominator in this expression shows that the largest contributions to the geometric phase arise when two Bloch bands are near each other. The geometric phase angle acquired by Bloch electrons is the source of the intrinsic component of the anomalous Hall effect [50] and the spin Hall effect [51]. Because the Berry curvature Eq. (2.19) acts as an effective magnetic field $\vec{B}_{eff}$, we write

$$\vec{J}_{Hall} = \frac{e^2}{\hbar}\vec{E} \times \langle \vec{B}_{eff} \rangle = \frac{e^2}{\hbar} E \langle \Omega \rangle \tag{2.20}$$

With $\vec{J}_{Hall}$ the Hall current of electrons or spins. So that

$$\sigma_{xy} = \frac{e^2}{\hbar} \langle \Omega \rangle \tag{2.21}$$

Therefore, in both cases the transverse conductivity of interest can be expressed as

$$\sigma_{xy} = \frac{1}{\hbar}\langle\Omega^n_{xy}(\vec{k})\rangle = \frac{1}{\hbar}\sum_{\vec{k},n} f(E_n(\vec{k}))\Omega^n_{xy}(\vec{k}) \tag{2.22}$$

where to obtain the average we sum over occupied bands n and momenta k weighted by the electron distribution function $f(E_n(\vec{k}))$. For the anomalous Hall effect case the operators of interest replacing $\partial_{k_{i,j}}H$ in Eq. (2.19) are the charge current operators $J_{x,y} = ev_{x,y}$, where e is the electron charge (this accounts for modifications of the equations by factors of e). For the spin Hall case we use instead a spin current operator $j^z_{s,x}$ [52] and a perpendicular charge current operator J_y.

2.4 Dzyaloshinskii-Moriya Interaction

The necessity of a spin-orbit coupling term of the form $D\vec{M}\cdot\left(\nabla\times\vec{M}\right)$ was first realized on the basis of symmetry arguments by Dzyaloshinskii [53] and later given a microscopic basis by Moriya [54]. However, it has recently been shown by Freimuth et al. that the DMI can be given a semiclassical [33] or perturbation theory [55] explanation in terms of the geometric phase discussed above.

The semiclassical explanation begins with consideration of a combined real-momentum space vector potential $\vec{A}(\vec{x},\vec{k})$. The curvature of such a vector field is described by a 6×6 curvature tensor

$$\Omega_{ij} = \nabla\times\vec{A} = \begin{pmatrix} \Omega^{xx} & \Omega^{xk} \\ \Omega^{kx} & \Omega^{kk} \end{pmatrix}_{ij} \tag{2.23}$$

The diagonal elements of this tensor are the matrices representing the pure real and momentum-space contributions to the vector potential curvature, which are the types

discussed in the preceding two sections. When considering the DMI we are concerned with the geometric phase acquired by electrons as they traverse a path that is closed when considered in the combined space $(\vec{x}, \vec{k})$, which is governed by the off-diagonal elements of Eq. (2.23). In chiral magnets like those studied in this dissertation, it is only these mixed-space contributions which are nonzero to first order in the spatial and momentum gradients of the system energy [33].

The change in free energy density due to the DMI can be written as

$$\delta F = D_{ij}\hat{e}_i \cdot \left(\hat{m} \times \frac{\partial \hat{m}}{\partial x_j}\right) \tag{2.24}$$

where repeated indices are to be summed over, $\hat{m}$ is the magnetization direction, and $\vec{x}$ is the position vector. Omitting (or obscuring by a $\tilde{f}$), for the sake of clarity, important terms and factors relating to the modification of energy levels and density of states by the geometric phase (see [33]) Eq. (2.24) becomes

$$\hat{e} \cdot \sum_n \int \frac{d^3k}{(2\pi)^3} \tilde{f}(E_n(k))\Omega^{xk}_{n,ij} \tag{2.25}$$

where now the Berry curvature is given by

$$\Omega^{xk}_{n,ij} = 2i\hbar \sum_{m \neq n} \frac{\langle u_{mk}| T_{i'} |u_{nk}\rangle \langle u_{nk}| v_j |u_{mk}\rangle}{(E_{mk} - E_{nk})^2} \left(\hat{m} \times \frac{\partial \hat{m}}{\partial x_i}\right)_{i'} \tag{2.26}$$

with T_i the torque operator $\vec{T}(\vec{x}) = \hat{m} \times \frac{\partial H}{\partial \hat{n}}$ (notice the summation over torque components). This result shows that the DMI coefficient is connected to the geometric phase in much the same way as the Hall conductivities in the previous section.

2.5 Skyrmions

2.5.1 General Model for Skyrmions

Adding the Dzyaloshinskii-Moriya term to the Heisenberg model for a ferromagnet with exchange and an external field gives an energy density [10]:

$$w = A(\nabla \vec{M})^2 - \vec{M} \cdot \vec{H} + D\vec{M} \cdot (\nabla \times \vec{M}) \tag{2.27}$$

If we consider a single skyrmion and treat its center as the center of a spherical coordinate system restricted to a plane with a radial coordinate ρ, we can write the direction of the magnetization at ρ as

$$\vec{m}(\rho) = \hat{x}\cos\phi(\rho)\sin\theta(\rho) + \hat{y}\sin\phi(\rho)\cos\theta(\rho) + \hat{z}\cos\theta(\rho) \tag{2.28}$$

where $\phi(\rho)$ and $\theta(\rho)$ are the polar and azimuthal angles of the magnetization. The polar angle is directly related to the azimuthal angle. For the materials studied in this thesis, $\phi = \pi/2 + \theta$ so fully describing the magnetization structure of the skyrmion requires only knowledge of its profile $\theta(\rho)$. With the coordinate system defined by Eq. (2.28), the energy density given by Eq. (2.27) can be written in the form [10]

$$w = 2\pi M^2 \left[A\left(\theta_\rho^2 + \frac{\sin^2\theta}{\rho^2}\right) + D\left(\theta_\rho + \frac{\sin 2\theta}{2\rho}\right) + \frac{H}{M}(1 - \cos\theta) \right] \rho \tag{2.29}$$

The Euler-Lagrange equation for $\theta(\rho)$ corresponding to this energy density is [56]

$$A\left(\theta_{\rho\rho} + \frac{1}{\rho}\theta_\rho - \frac{1}{2\rho^2}\sin 2\theta\right) - \frac{H}{2M}\sin\theta - \frac{D}{\rho}\sin^2\theta = 0 \tag{2.30}$$

Defining $h = H/AM$ and $d = D/A$ lets us write

$$\theta_{\rho\rho} + \frac{1}{\rho}\theta_\rho - \frac{1}{2\rho^2}\sin 2\theta = \frac{h}{2}\sin\theta + \frac{d}{\rho}\sin^2\theta \tag{2.31}$$

The boundary condition is that $\theta(0)$ must differ from $\theta(\infty)$ by π. This equation is not integrable and there is no known exact analytical solution for $\theta(\rho)$. Currently, numerical methods are used to obtain the skyrmion profile function. However, it is possible to make simple approximations to the magnetization profile as ρ approaches 0 or ∞ and there are expressions which approximate the full profile, including one which has been overlooked previously (discussed in Chapter 7) in the context of the radially symmetric skyrmions relevant for chiral magnetic materials and thin ferromagnets.

2.5.2 Approximations to the Skyrmion Profile

First, it is illuminating to consider Eq. (2.31) with its right-hand side set to 0:

$$\theta_{\rho\rho} + \frac{1}{\rho}\theta_\rho - \frac{1}{2\rho^2}\sin 2\theta = 0 \tag{2.32}$$

In this case it constitutes a system called an O(3) nonlinear sigma model without any potential terms. It possesses exact radially symmetric soliton [57, 27] solutions, first discovered in the context of isotropic ferromagnets by Belavin and Polyakov, whose profiles have the form [34]:

$$\theta(\rho)_L = 2\arctan\left(\frac{R}{r}\right) \tag{2.33}$$

where R determines the size of the soliton.

It is clear from physical arguments that these solitons cannot be stable structures in

a (classical) magnetic system because the sigma model under discussion describes a Heisenberg model with magnetic exchange only, so that the state of minimum energy must have all spins aligned (θ equal to π or 0 for all ρ). A question arises in that the skyrmion number (Eq. (2.1)) of the lump soliton is 1 ($\cos\theta(\infty) - \cos\theta(0) = 2$) so one might think that it should be topologically protected in the same way that the skyrmion is. However, since the size of the soliton is arbitrary (Eq. (2.33) solves Eq. (2.32) for any R) there is nothing preventing it from expanding to infinity or shrinking to zero size, making it unstable. This instability has been demonstrated numerically (e.g. [58]).

Despite the possibility of obtaining numerical solutions to the skyrmion profile equation Eq. (2.31), it is often preferable to seek analytic approximations both to save time and to obtain physical insight that may not be available from the numerical solution. Sometimes the expression [59]

$$\theta(\rho)_L = \arccos\left(\frac{(r/R)^{2n} - 1}{(r/R)^{2n} + 1}\right) \tag{2.34}$$

where n is the number of skyrmions has been used as an approximation for the profile function of 2D skyrmions in analogy with the rational map ansatz/approximation for full 3-dimensional skyrmions. However, for single skyrmions ($n = 1$) the approximation is equivalent to Eq. (2.33) and therefore has a power law rather than exponential approach to 0 as $\rho \to \infty$. The stability is improved for the approximation compared to the exact solution for the O(3) model discussed above because generally the right hand side of Eq. (2.31) is not zero. The approximation Eq. (2.34) was shown numerically [59] to be more suitable for multiskyrmion ($n > 1$) solutions than for the single skyrmion case.

Another approximation, which prioritizes the large ρ behavior of the skyrmion profile

is given by [60]:

$$\theta(\rho)_B = K_1(\rho/R) \tag{2.35}$$

Where $K_1(x)$ is the order one modified Bessel function of the second kind (also known as a Macdonald function). Since the $\rho \ll R$ behavior of this approximation is incorrect, it is only used as a starting point for numerical approximations or to model behavior far from the skyrmion center (which it does well [16]). Another common approach is to model the skyrmion profile as strictly linear near the center and exponential far away as was done in (e.g.) [35]. In Chapter 7 I present an improved approximation for the profile of a single skyrmion.

Chapter 3

Electrical Detection of Skyrmions

3.1 Other Observation Approaches

The original studies which confirmed the existence of a skyrmion crystal structure in B20 materials were small angle neutron scattering (SANS) measurements [12]. Such measurements are restricted to either bulk samples or relatively thick films to provide sufficient signal and, importantly, SANS is a reciprocal space measurement so while it does probe magnetization it only does so for a crystal of skyrmions and is not suitable for studying nanodevices. Magnetic force microscopy, which relies on the measurement of stray magnetic fields rather than directly probing magnetization structure has so far [61] exhibited barely sufficient spatial resolution to indicate the presence of skyrmions but cannot image (and confirm) their novel structure. High spatial resolution scanning probe magnetometry [62] of the stray fields due to a skyrmion using a diamond nitrogen-vacancy sensor is very promising but has not yet been realized. A magnetization-sensitive scanning-probe measurement technique which has been applied to study skyrmions in real space is spin polarized scanning

tunneling microscopy (SP-STM) [63]. These measurements, while highly resolved, are very delicate and difficult and the equipment is costly to operate, it would probably not be suitable for even moderate volume testing of materials and devices for skyrmion-based technological applications. Additionally, since they have only been applied to very thin (one or two monolayer) ferromagnetic layers, their suitability for measurements on thicker B20 helimagnets at higher temperatures is unknown. This brings us to consideration of Lorentz transmission electron microscopy (LTEM) [64], the most convincing current technique for studying skyrmions in real space as well as the first to have provided real space images of them [15]. The problems with this technique stem from intrinsic difficulty and the sample preparation needed. LTEM observations of skyrmions have typically been carried out on thinned single crystals of B20 helimagnet materials though the technique has been used on an MBE deposited thin film [65] and chemical vapor deposited (CVD) single-crystal nanowires [66] of MnSi (after thinning by focused ion beam). In all cases LTEM requires both very thin and very flat samples making it problematic for studying skyrmions in devices with structures more complicated than a wire and requiring painstaking thinning and preparation of samples using additional equipment. Also, transmission electron microscopes with sufficient flexibility to carry out the measurement are not very common and in particular the software needed to reconstruct the Lorentz TEM images can be costly and challenging to implement, to the point that only one group [15, 66, 67] has consistently performed the measurement.

3.2 Electrical Measurements

Electrical measurements are relatively accessible and most (though not all [68, 69, 70]) agree that they can provide convincing evidence for the presence of skyrmions in thin

films. In this thesis (Chapter 6), work on measuring the topological Hall effect and longitudinal transverse magnetoresistance, both described below, in thin films of MnSi is presented.

3.2.1 Topological Hall Effect

A skyrmion lattice (Fig. 1.2) is an extended smoothly varying magnetization structure. When a current of conduction electrons passes through this background it experiences an effective magnetic field due to the geometric phase acquired by the electrons during their passage. In terms of the local magnetization vector and its spatial derivatives this effective field is given by [71]:

$$B_{eff} = PR_0 \frac{h/e}{4\pi} \int \vec{m} \cdot \left(\frac{\partial \vec{m}}{\partial x} \times \frac{\partial \vec{m}}{\partial y} \right) d\Omega \tag{3.1}$$

Where P is the polarization of the electron current (relative to the background magnetization outside of the skyrmions) and R_0 is the normal Hall effect coefficient. This is just a constant factor multiplying the topologically invariant skyrmion number N_{sk} of Section 2.1. The factor P is present because oppositely polarized electrons acquire opposite real-space geometric phases during their passage.

It is best to think of the whole many-electron current interacting with this effective field because in chiral ferromagnets (Ch. 4) the skyrmion is much larger than an electron (accounting for the adiabatic nature of the interaction between the magnetization and the electron current which is a condition for the acquisition of a geometric phase) so that the effects of the field are seen as the average of many individual scattering events. The net result of these events is the addition of a perpendicular component to the electron transport. This is on top of the ordinary Hall effect due to the applied field which is typically needed to stabilize the skyrmion lattice and the

anomalous Hall effect which is the dominant contribution to perpendicular electrical transport at low magnetic fields in chiral ferromagnets like MnSi. Typically, it is easiest to consider measurements in terms of a Hall resistivity which can be written out in terms of its components as [71]

$$\rho_{xy} = R_0 H + \rho_{xy}^{AHE} + \rho_{xy}^{t} \tag{3.2}$$

Where H is the applied magnetic field, R_0 is the normal Hall resistance, ρ_{xy}^{AHE} is the anomalous Hall effect contribution, and ρ_{xy}^{t} is the topological term arising from the effective magnetic field B_{eff} of Eq. (3.1). In MnSi, the second term can be taken to have the form [72]

$$\rho_{xy}^{AHE} = S_H \rho_{xx}^2 M \tag{3.3}$$

The way in which ρ_{xy}^{t} is usually extracted [65] is to measure ρ_{xy} over a wide field range and use knowledge of ρ_{xx} and M to obtain the values of R_0 and S_H by fitting the data above the critical field for the existence of skyrmions where ρ_{xy}^{t} is expected to be zero.

The first electrical detection of skyrmions [71] was accomplished in this way. Transport experiments [73] have shown the stepped change in the topological Hall resistance as skyrmions are added to and removed from a nanowire of FeGe so it is clear that electrical transport measurements of this kind are sensitive to the number of skyrmions present as expected from Eq. (3.1).

3.2.2 Longitudinal Magnetoresistance

A less established indicator of the presence of skyrmions is a minimum in the longitudinal magnetoresistance measured in the plane of the sample with the magnetic field

applied perpendicular to that plane. The origin of this minimum is not fully understood but is suspected to be topological in nature just as the topological Hall effect is [74, 75]. What is clearly observed is that in each case where both electrical and LTEM measurements have been carried out, whether in bulk single crystals [75, 76], single crystal nanowires [77, 66], or epitaxial thin films [65], a minimum in magnetoresistance always coincides with the presence of skyrmions. For the measurements described in this thesis (as well as the studies just mentioned) the applied magnetic field is always perpendicular to the plane of the film, or nanowire (in the <111> direction, and also in this direction in single crystal samples). The current is in the plane of the sample, so this is a transverse magnetoresistance measurement, and the voltage is measured parallel to the applied current so it is a longitudinal resistance measurement.

Yi *et al.* [74] found that in chiral ferromagnetic materials

$$\sigma_{xx} = \frac{1}{\hbar} \sum_{\vec{k},n} f(E_n(\vec{k}))\Omega^n_{xx}(\vec{k}) \tag{3.4}$$

Where the curvature $\Omega^n_{xx}(\vec{k})$ is given by

$$\Omega^n_{xx}(\vec{k}) = 2i\eta \sum_{m \neq n} \frac{|\langle u_{nk}| J_x |u_{mk}\rangle|^2}{\eta^2 + (E_{mk} - E_{nk})^2} \cdot \frac{1}{E_{mk} - E_{nk}} \tag{3.5}$$

This is very similar to Eq. (2.19) except that for the longitudinal case the relaxation parameter $\eta \sim \frac{1}{\tau}$ [50] (where τ is the transport lifetime) cannot be ignored, and is in fact required for a finite longitudinal conductivity. This can be thought of as a Berry curvature dependent contribution that can only arise from scattering of the electrons into states with momenta parallel to the original (longitudinal) current (i.e. it arises from conduction electrons slowing down). This contribution is even more dependent on the energy separation between bands than the Hall currents. Like the

Hall current, it should be sensitive to a Berry phase arising from the presence of skyrmions. Unfortunately, testing this would require band structure calculations for MnSi and quantitative comparison with transport measurements which is beyond the scope of this thesis.

The work of Demishev *et al.* [78] on anisotropy of magnetoresistance in single crystals of MnSi supports the contention that this measurement can provide accurate information about the presence of skyrmions.

Chapter 4

Chiral Ferromagnets

4.1 B20 Crystal Structure

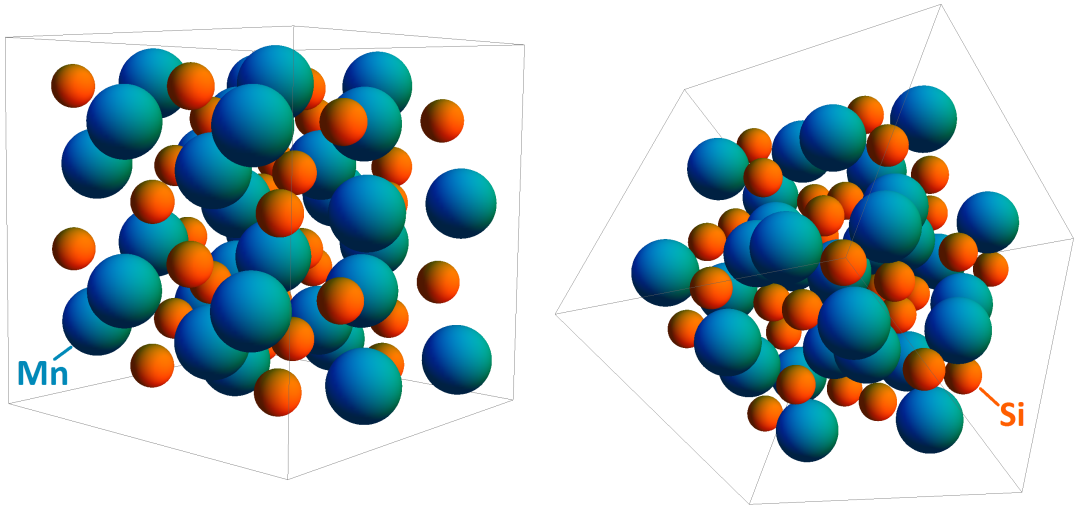

(a) (b)

Figure 4.1: B20 cubic Crystal Structure: (a) Arbitrary side view. (b) View along the <111> axis showing the structure's intrinsic chirality. We take MnSi as a prototypical example and label the atoms.

The B20 crystal structure (see Figure 4.1) is a non-centrosymmetric cubic structure of

the $P2_13$ space group. By re-orienting one's view of the crystal (Fig. 4.2(b)) the helical structure along the <111> axis becomes clear. The broken symmetry arising from this structure is the cause of the strong bulk Dzyaloshinskii-Moriya interaction. The unit cell of the crystal (Fig. 4.2) can be thought of as consisting of two interpenetrating tetrahedra of the transition metal(s) and the Group IV (only Ge or Si for the magnetic materials we study, but (e.g.) PtAl also has the B20 structure) atoms. These two tetrahedra are counter-rotated with respect to each other resulting in the break in symmetry. For the magnetic behavior of these materials which is focused on here, we are always concerned with the magnetic atoms only.

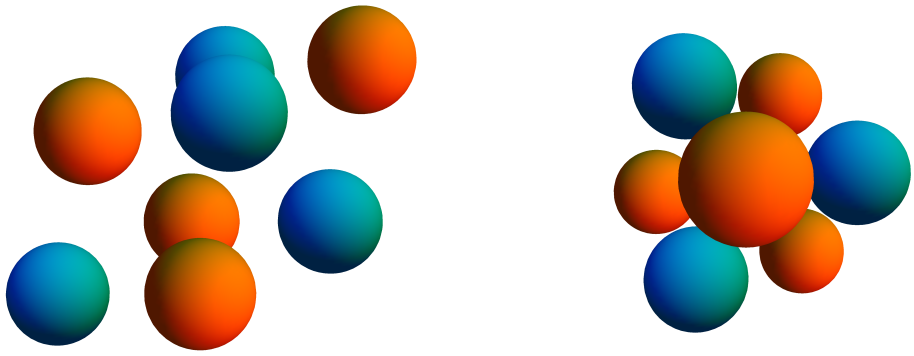

(a) (b)

Figure 4.2: Unit cell of a B20 cubic structure. (a) Arbitrary side view. (b) Along <111> direction.

Initially, skyrmions were only observed in $P2_13$ space group materials though very recently materials with a different type of structure [79] and thin ferromagnetic films taking advantage of interfacial DM interaction [80] have apparently exhibited the presence of skyrmions.

4.2 States in B20 Ferromagnets

There are three states which can arise in helical magnets at ambient pressure: a weakly ferromagnetic state in which the spins are arranged helically, a high temperature paramagnetic state where the spins align with any external field, and in some sense "between" these, a skyrmion phase, arising from a competition between helical and ferromagnetic alignment.

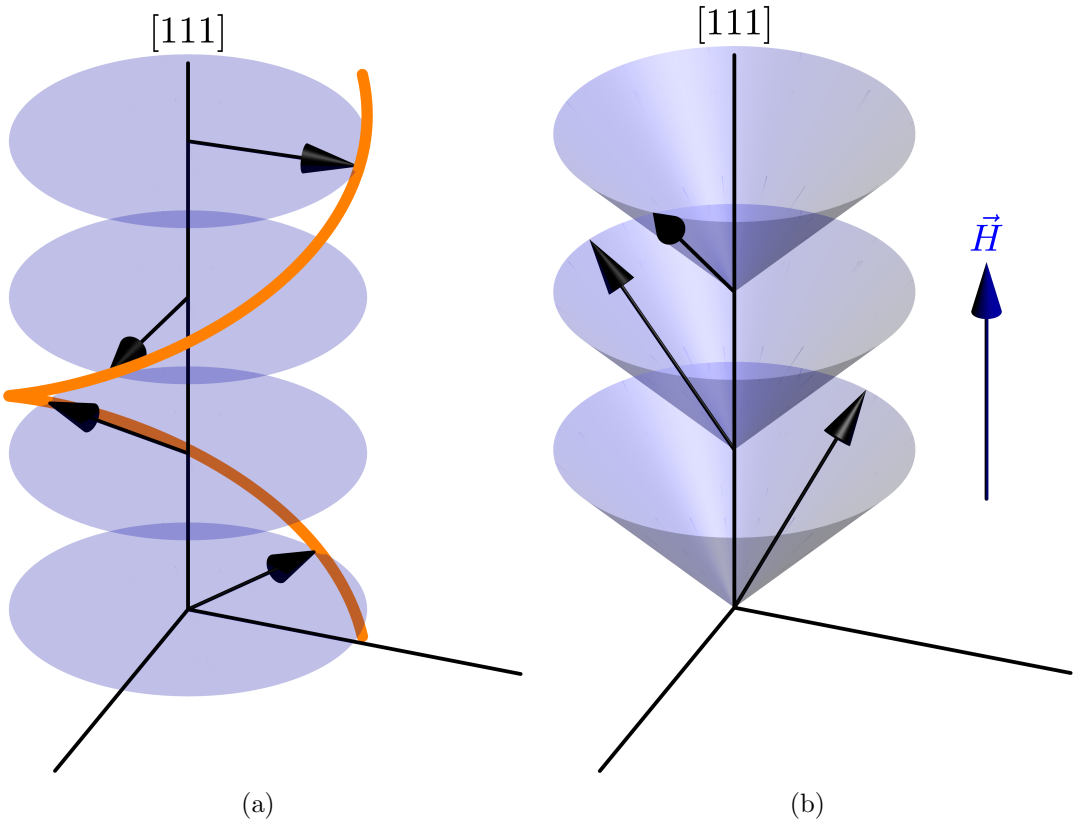

Figure 4.3: (a) Helical magnetization configuration. (b) Conical magnetization configuration.

4.2.1 Helimagnet

The Dzyaloshinskii-Moriya interaction favors the formation of a helical magnetic state with its axis oriented along the <111> direction and diameter $A/|D|$ and pitch $k = |D|/2A$ where D is the Dzyaloshinskii constant and A is the exchange constant. The helical magnetization structure is given by

$$\vec{M} = M\left[\vec{n}_1 \cos(\vec{k}\cdot\vec{r}) + \vec{n}_1 \cos(\vec{k}\cdot\vec{r})\right] \tag{4.1}$$

Here $\vec{n}_i$ are orthogonal unit vectors in the plane of the magnetization. A short portion of such a structure is shown in Fig. 4.3(a). This is the typical ground state configuration of B20 ferromagnets and so it is the zero-field, low-temperature (below the Curie temperature) phase.

4.2.2 Conical Phase

As the applied magnetic field is increased the spins in the initially helimagnetic material are rotated out of the plane and toward the <1l1> axis (see Fig. 4.3(b)). The opening angle θ between the magnetization vector and the applied field H is given by $\cos\theta = H/H_D$ where $H_D = D^2M/(2A)$ is the saturation field for the helimagnetic state [56].

4.2.3 Paramagnet

Above the Curie temperature these materials behave as paramagnets and all spins will align to any applied field. This phase is topologically trivial.

4.2.4 Skyrmion

A skyrmion is a knot of magnetization which to a good approximation can be thought of as a cross or combination between a domain wall and a vortex, perhaps best explained by an image of their structure (Fig. 1.1). Further details and properties of individual skyrmions were discussed in Chapter 2 and here we are most concerned with the behavior of the skyrmion *state* of chiral ferromagnets.

In bulk, single crystal samples of B20 ferromagnets, skyrmions only arise in a very restricted region of T-H space, just below the Curie temperature. The period of this lattice is the same as the pitch of the helical magnetic state which precedes it and this crystal of magnetization is therefore much larger than the atomic lattice which underlies it. In an extreme case, the skyrmion lattice in FeGe has a period of $70nm$ while the lattice parameter of cubic FeGe is 4.68 Å. The skyrmions form lattices of such regularity that they can be observed in neutron diffraction [12]. These hexagonal lattices greatly resemble the Abrikosov lattice [81] of vortices in high-temperature superconductors.

The transitions both from cone phase to skyrmion crystal and from skyrmion crystal to paramagnet are first order. As field or temperature is increased, the skyrmion crystal "melts" into clusters and eventually individual skyrmions [15]. It is currently unclear how the three intersecting helix model, which has been used so successfully to explain neutron diffraction data pertaining to skyrmion crystals, appropriately describes their behavior as these crystals break up. Unfortunately there are no direct observations of the skyrmion lattice "freezing" into place. However, individual skyrmions and clusters have been observed at junctions of helical domain walls in the helimagnet FeGe [67].

Chapter 5

Material Deposition and Device Fabrication

5.1 Magnetron Sputtering

Sputtering works by using an argon plasma to strike (sputter) surface material from targets. The mixed plasma then deposits on a stage which holds a substrate on which the material of interest is grown (as well as the walls of the vacuum chamber). Deposition time is controlled via shutters over the targets. The stage is usually rotated to promote uniformity of deposition and may also be heated (as it was for the samples grown in this research). The advantages of this deposition method are a high degree of uniformity and the possibility of thoroughly mixing co-deposited materials as well as relatively high deposition rates while still maintaining the possibility of highly textured (ordered), low material stress, and even epitaxial growth.

In the DC case (used for the materials described in this thesis), the Ar ions are drawn to the metallic target because it is held at a constant negative voltage. A magnetron

consisting of permanent magnets incorporated in the structure supporting and charging the target (together called a "source") with one magnetic pole in the center and the other pole distributed under the outer edge of the target (all discrete cylindrical permanent magnets) was used in all the depositions described. This configuration produces crossed electric (perpendicular to target surface) and magnetic (radial from target center) fields near the surface of the target resulting in a drift velocity (known as the $\vec{E} \times \vec{B}$ drift in plasma physics [82])

$$\vec{v_{\perp}} = \frac{\vec{E} \times \vec{B}}{B^2} \tag{5.1}$$

Which with the present field orientations will tend to produce a circulation of the plasma near the surface of the target, resulting in more sputtering.

The particular sputtering system used (an AJA International ATC Orion with A300 series sputtering sources) was also equipped with the capability of igniting an RF Argon plasma on the stage, providing a means of cleaning or even etching away the surface of the substrate.

The main parameters available to control the characteristics of the deposition and the material produced are substrate temperature, argon gas pressure, and voltage (or equivalently power) applied to the target. The RF cleaning time and power can also be important for achieving particular substrate characteristics. In all growth procedures described below the sputtering system base pressure was 1×10^{-8} Torr or less.

5.2 Material Deposition

5.2.1 MnSi

For growth of MnSi, a substrate of <111> oriented undoped Si (MTI Inc.) was used. The surface oxidation layer was removed by RF sputtering with a power of 40W and an Ar pressure of 20 mTorr for 7 minutes. After this the stage was heated, with temperature stabilized in 100 °C steps and finally stabilized at a target temperature between 275°C and 375°C with an optimal temperature of 325°C. The growth did not require high temperature reconstruction of the Si surface structure in order to succeed. The substrate was held at this temperature while MnSi was deposited from a stoichiometric target (Kurt J. Lesker). The MnSi deposition characteristics were 15W deposition power, and 2 mTorr Ar pressure. The heating was then turned off and the sample was allowed to cool to room temperature in vacuum.

MnSi on AlOx

It can be desirable to protect an etched Si<111> surface from natural oxidation in air with some material that would still allow B20-structured MnSi to be deposited. This was accomplished by depositing 3nm of Al at 45W on the Si surface after it had been etched by Ar plasma as described above. The etching and deposition were carried out at room temperature. The coated substrate was then removed from the vacuum chamber and allowed to oxidize in air for >3 days. Afterwards, the MnSi was deposited on the resulting amorphous aluminum oxide using the same procedure as above with only light RF plasma cleaning (15W, 40s). The entire sample then had to be annealed at 700° to produce the structured MnSi film.

MnSi on Ta

Since it turned out to be possible to deposit cubic MnSi (albeit only structured in-plane (see Ch. 6)), many other underlayers were tried. The most successful of these was a $5nm$ layer of tantalum deposited at a DC power of 75W on Si<111> substrate etched as described above. Ta deposition was done at room temperature and MnSi was deposited according the process described above and without the need for additional high-temperature annealing.

5.2.2 FeGe

Depositing cubic (B20) FeGe directly on Si<111> was not successful under any of various conditions attempted (Ar pressures of as little as 1 mTorr, substrate temperatures from room temperature to 700°C, and DC power from 15W to 45W, with and without attempted Si surface reconstruction) in all cases there was significant (50%) mixture of hexagonal FeGe. This is in contrast to the results of Huang and Chien [83] who were able to deposit high-quality FeGe at 500°C directly on Si<111>. This may indicate that HF chemical etching as used in [83] is beneficial for FeGe growth when compared to Ar plasma etching for Si substrate preparation. Depositing this material was also not successful on a thin layer of FeSi grown on the Si<111> substrate.

Instead, B20 FeGe was deposited on Ar plasma thinned layers of the MnSi films whose deposition was described in the preceding subsection. Films of 20nm thickness were etched by RF sputtering at 40W with an Ar pressure of 20 mTorr for 8 minutes at room temperature. FeGe from a stoichiometric target was deposited at 425°C after step by step substrate heating and temperature stabilization. The deposition conditions were 45W source power and 2 mTorr Ar pressure. Again the sample was allowed to cool freely in vacuum.

Neither of the targets (MnSi and FeGe) are very good conductors so the targets consisted of .125" thick × 2" diameter of the desired material in stoichiometric mixture mounted with indium on a .125" thick × 2" diameter copper piece. It is very important that the applied DC power be kept low ($\leq$ 60W for MnSi and $\leq$ 45W for FeGe) to avoid the possibility of damaging the target and/or melting indium and shorting the source.

5.3 X-Ray Diffractometry

Here we will briefly describe the XRD characterization techniques used to study the materials deposited. The results of these studies of our samples will be presented in the next chapter. For ideal (nondispersive), unpolarized X-rays of angular frequency ω incident on a crystal, the fraction of incident light intensity diffracted into an angle dΩ is [84](Ch.15)

$$d\sigma = \frac{1}{2}\left(\frac{e^2}{mc^2}\right)^2 \left(1 + \frac{c^4}{\omega^4}(\vec{k}' \cdot \vec{k})^2 \left| \int n e^{-i(\vec{k}'-\vec{k})\cdot\vec{r}} dV \right|^2 \right) d\Omega \tag{5.2}$$

where $\vec{k}$ and $\vec{k}'$ are the incident and scattered wave vectors respectively and n is the local electron density at position $\vec{r}$ which can be expanded over the periods $\vec{b}$ of the reciprocal lattice as

$$n = \sum_b n_b e^{2\pi i \vec{b}\cdot\vec{r}} \tag{5.3}$$

showing that $d\sigma$ decreases exponentially except where

$$\vec{k}' - \vec{k} = 2\pi\vec{b} \tag{5.4}$$

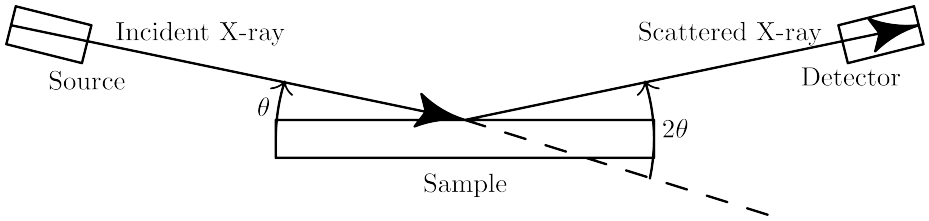

Figure 5.1: Schematic of X-ray diffraction measurement for 2θ-ω or grazing incidence.

is satisfied. This gives an indication of the utility of the X-ray diffraction pattern for determining the crystal structure in reciprocal space as defined by the various $\vec{b}$. This result was due to von Laue and can be rewritten (because $k = \omega/c = pi/\lambda$) as the Bragg equation:

$$k \sin\theta = \frac{n\pi}{d} \Rightarrow 2d \sin\theta = n\lambda \tag{5.5}$$

where θ is the angle between $\vec{k}'$ and the crystal plane (perpendicular to $\vec{k}' - \vec{k}$) and $d = 1/b$ is the distance between lattice planes in the family defined by $\vec{b}$ [85]. The output of an X-ray diffractometer is a diffraction pattern consisting of an intensity versus θ or 2θ curve possessing various peaks which correspond to values of θ for which the Bragg condition for some lattice spacing d is satisfied. In powdered samples, crystallites are present in all orientations so all possible crystal peaks are obtained for all scans. For the thin film samples studied here, which may be at least partly epitaxial, the orientation of the sample with respect to the x-ray beams can be important because peaks from crystal planes parallel to the incident x-ray will never be resolved.

5.3.1 2Theta-Omega Measurements

One useful technique for phase (crystal structure) identification in thin films is referred to as a $2\theta - \omega$ scan and is carried out by moving both the X-ray source and the detector (see Fig. 5.1) through various angles with respect to the plane of the sample. In this configuration, the incident beam reaches relatively large angles and so probes deeply

into the sample, obtaining significant information about crystal planes parallel to the surface. One downside of this approach is that the substrate material is heavily sampled and is both thicker and usually more perfectly ordered than the thin film deposited on it so that substrate peaks can dominate over the signal of interest. Also, the orientation is incorrect for studying crystal planes perpendicular to the sample surface and will return little signal from them.

5.3.2 Grazing Incidence Measurement

One way to deal with the problems inherent in the $2\theta - \omega$ measurement is to carry out a complementary Grazing Incidence X-Ray Diffraction (GIXRD) measurement on the sample. In this type of measurement the orientation of the incident X-ray remains fixed at a small angle ($\theta < 1^{\circ}$) nearly parallel to the sample while the detector is scanned through a range of angles. This measurement complements the $2\theta - \omega$ scan in that it mostly misses the substrate and gives information about planes perpendicular to the sample surface (though not exclusively such planes). GIXRD can also allow one to obtain data from samples that might be too thin to give enough signal for a $2\theta - \omega$ measurement since light can be scattered from sites all along the length of the sample, though measuring very thin (<5nm) films can be difficult to carry out in practice.

Usually, a combination of a GIXRD and a $2\theta/\omega$ measurement is sufficient to identify the phase of a material under study or at least to determine if it is indeed a target material phase.

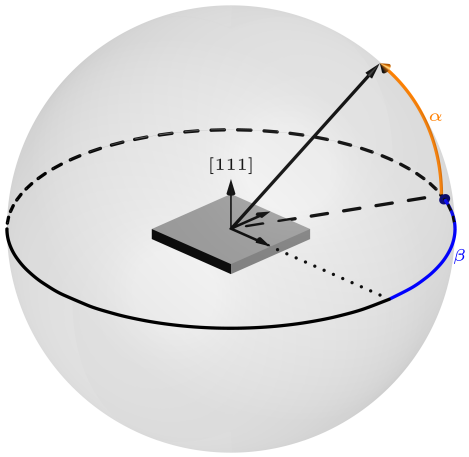

Figure 5.2: Schematic showing the coordinates for a pole figure measurement.

5.3.3 Pole Figure Measurement

Once a sample material is identified it can be further characterized by carrying out a pole figure measurement. This measurement is particularly useful for determining the sample's "texture". By texture we mean the degree to which the crystallites of which a polycrystalline sample is composed are aligned with each other. This ordering can differ depending on direction.

In a pole figure measurement [86], a particular crystal plane is selected (so a $2\theta/\omega$ measurement must be carried out first) and its normal is used as the axis of a hemisphere measurement sweeping over a polar angle usually labeled α and azimuthal angle β (see Fig. 5.2). For this work, the pole figure was measured about the [111] axis which was well aligned with the film normal (as shown in the figure) but the measurement is the same even when this is not the case. The detector is fixed at a specific 2θ position (corresponding to a peak, for our work this was always the <111> peak of the material of interest). The sample is then rotated in the plane (β-scan) and tilted out of the plane (α-scan) to record pole figure data. In the Rigaku Smartlab XRD of the LEXI facility at UC Irvine where these measurements were carried out,

standard pole figure measurement requires the sample stage to be rotated up to 90 degrees out of plane so that it is necessary to fix the sample to the stage. This was accomplished by affixing the sample to a glass slide using double-sided carbon tape and subsequently using scotch tape to attach the slide to the sample stage. This was sufficient to keep the sample stable throughout the measurement and no additional distortion was observed in the acquired data. It is also possible to obtain the same data without tilting the sample by simultaneously varying the out of plane angle of the source and the in-plane (azimuthal) angle of the detector, while still maintaining the same fixed 2θ angle. This is known as an in-plane pole figure measurement.

The resulting data is either plotted on a sphere or projected stereographically onto a polar plot (see Chapter 6). It gives information about the crystal texture, which can be an indicator of its quality and affects its physical properties. It also provides additional evidence regarding the overall structure of the crystal being investigated (e.g. the pole figures of even partially ordered hcp and bcc crystals would be difficult to confuse with each other).

5.4 Device Fabrication

Devices for transport measurements on MnSi thin films were fabricated by two different methods. Early MnSi samples were given a four-contact measurement structure (see figure in Chapter 6) using a molybdenum shadow mask during deposition. The mask was fixed to the surface of the substrate using metal clips prior to loading into the sputtering system.

Later devices were fabricated in a Hall cross pattern in order to make better transverse conductivity measurements. These devices were patterned by e-beam lithography us-

ing the negative-tone electron beam resist hydrogen silsesquioxane (HSQ) (DOW Corning XR-1541). HSQ interlinks relatively quickly under ambient conditions, making it impossible to pattern after approximately two to three hours. As time from spin-coating approaches this limit it becomes increasingly difficult to pattern small features with high resolution. For relatively large structures like the devices studied in this thesis, these conditions can still pose problems because HSQ requires high doses of electrons ($>1000\mu C/cm^2$), meaning that writing a large device at a low electron beam current could easily take more than the time available to write on HSQ. The solution (for large devices) is to carefully go to higher currents. In the course of this work it became clear that it was possible to use quite large e-beam currents to write large structures in HSQ with no apparent ill effects.

For the devices measured, resist was spin-coated onto MnSi films at 5000 rpm for 60 seconds followed by a 120 second bake at 250°C on a hot plate. The coated samples were loaded into a scanning electron microscope (FEI Magellan 4XHR with e-beam writing controls by Nabity-NPGS) within 10 minutes of spinning. Hall cross devices of width $1\mu m$ and arm length $5\mu m$ were patterned with an SEM beam voltage of 30kV at a beam current of 100 pA and a dosage of $2500\mu C/cm^2$ (Fig. 5.3(a)). Smaller devices with a width of $300nm$ and an arm length of $500nm$ were patterned with a beam current of 25 pA and a dosage of $1800\mu C/cm^2$ (Fig. 5.3(b)). This demonstrates that the thin film etching technique developed here is suitable for making small devices.

After writing, samples were post-baked for two minutes at 250°C on a hot plate followed by development at room temperature in MF-319 for 30 seconds and rinsed in HPLC grade water for 60 seconds under a continuous stream from a squeeze bottle. For future researchers who may work with HSQ and this development procedure, I wish to point out that MF-319 is really 2.5% tertmethylammonium hydroxide (TMAH) which in its more concentrated 25% solution is treated as being almost on

par with HF in its inherent danger, in that its use is often segregated to particular equipment/areas in clean rooms and requires special/enhanced protective equipment. The concentrated form is acutely toxic (occasionally to the point of fatality) with skin exposure (as well as highly corrosive) and the low concentration we use has demonstrated acute toxicity with large-area skin exposures. There is no reason that the concentration we use cannot be used safely within our own lab but like all chemicals it should be treated with respect.

Following the formation of the HSQ pattern (which becomes essentially glassy SiO_2) on the surface of the film, it is imaged using the same SEM used to write the pattern. Good imaging conditions for these devices are around 7kV and 25 - 50pA.

The last step in sample fabrication is etching of the sample by ion milling. The sample is fixed to a piece of carrier wafer using vacuum compatible thermal grease with its patterned face exposed. This is then loaded onto a sample stage which is tilted to face an ion beam at a particular angle. In the case of the samples studied in this thesis, the angle was 45°. A shutter was used to set up a 25% duty cycle of beam exposure with every 15 seconds of exposure followed by 45 seconds of shadow. The device is exposed for a total of 120 seconds to remove the material not protected by developed HSQ. The beam characteristics were an acceleration voltage of 80V with a beam voltage of 400V. The resulting devices are shown in Fig. 5.3.

The Hall crosses used for the electrical measurements discussed in Chapter 6 are fabricated, including leads, following the procedure described above for a large Hall cross ($1\mu m$ width) with the addition of lead and contact pad defining steps during e-beam writing. The inner lead structures are written with a current of 100 pA and a dosage of 1800 $\mu C/cm^2$ while the outermost structures (contact pads) are written at beam currents of 6400 pA and a dosage of $2100\mu C/cm^2$. The whole structure is then developed as described above and ion milled for 135 seconds under the same

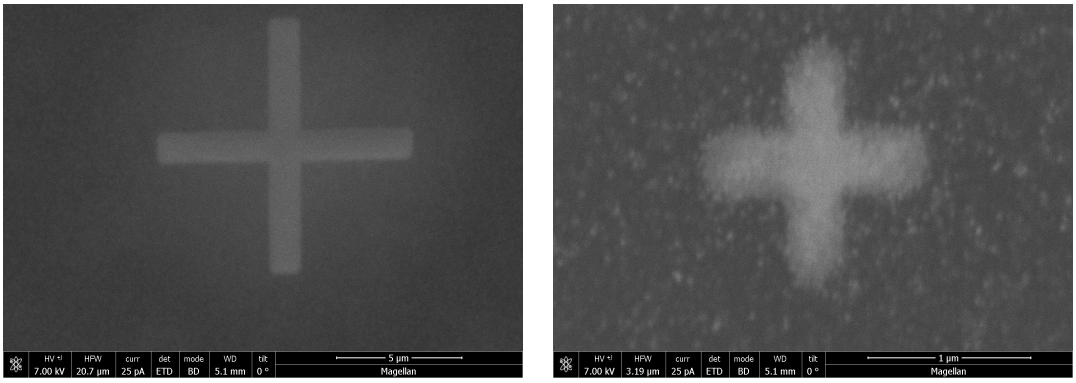

(a) (b)

Figure 5.3: (a) Large Hall cross etched with ion beam. (b) Small Hall cross etched with ion beam.

conditions described for the crosses alone (25% duty cycle, 80V acceleration voltage and beam voltage 400V). The device is shown in Figure 5.4.

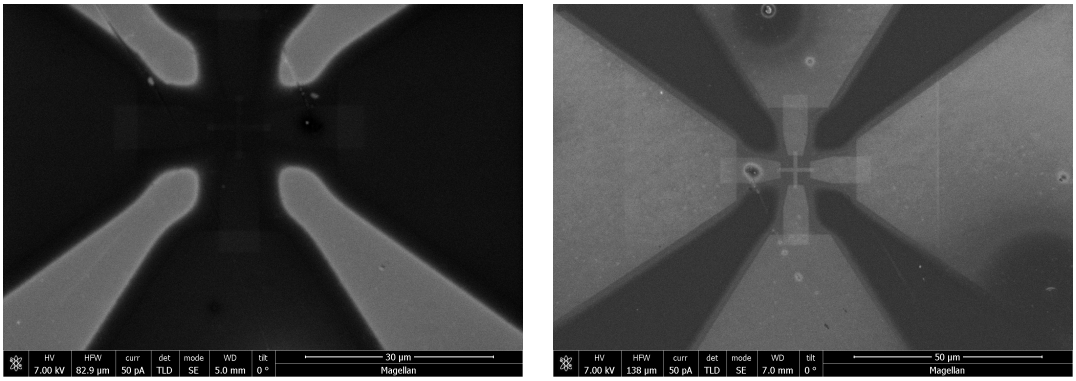

(a) (b)

Figure 5.4: (a) Before ion milling. (b) After 135s milling.

Later, larger full six-contact Hall bar devices were patterned under the same conditions as the outer portion of the contacts described above (6400 pA and a dosage of $2100\mu C/cm^2$) (Fig. 5.5). Ion milling for these structures was the same as for the combined Hall cross/contact structure described above (25% duty cycle, 80V acceleration voltage and beam voltage 400V) but with a longer etch time (200s).

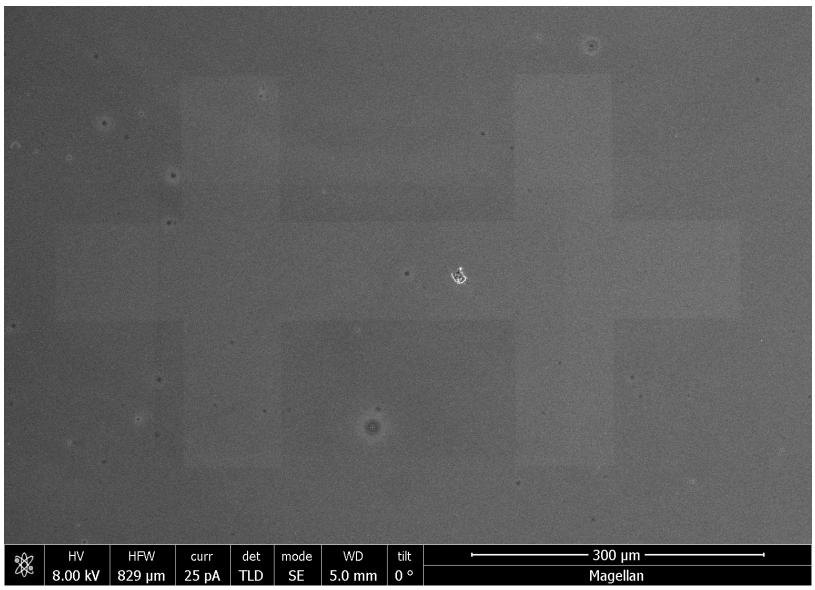

Figure 5.5: MnSi Hall bar after 200s ion milling.

Chapter 6

Results

6.1 XRD Characterization

Characteristics of the films deposited and degree of success in growing the target materials were determined by x-ray diffractometry (see section 5.3). In particular for MnSi we especially seek a unique peak for <111> MnSi at 2θ =34° and the absence of contamination by Mn_5Si_3 and $MnSi_{1.7}$.

6.1.1 MnSi

Figure 6.1 shows the high angle and grazing-incidence XRD traces for MnSi sputter deposited as described in Section 5.2.1. For failed growth procedures the competing phases $MnSi_{1.7}$ (temperature too high or deposition too slow) or Mn_5Si_3 (temperature too low or deposition at too high a power) indicated in the figure will be present. The presence of a small <210> peak in the $2\theta/\omega$ spectrum indicates that while the film is high ordered in the out of plane direction (see below for pole figure data), there is

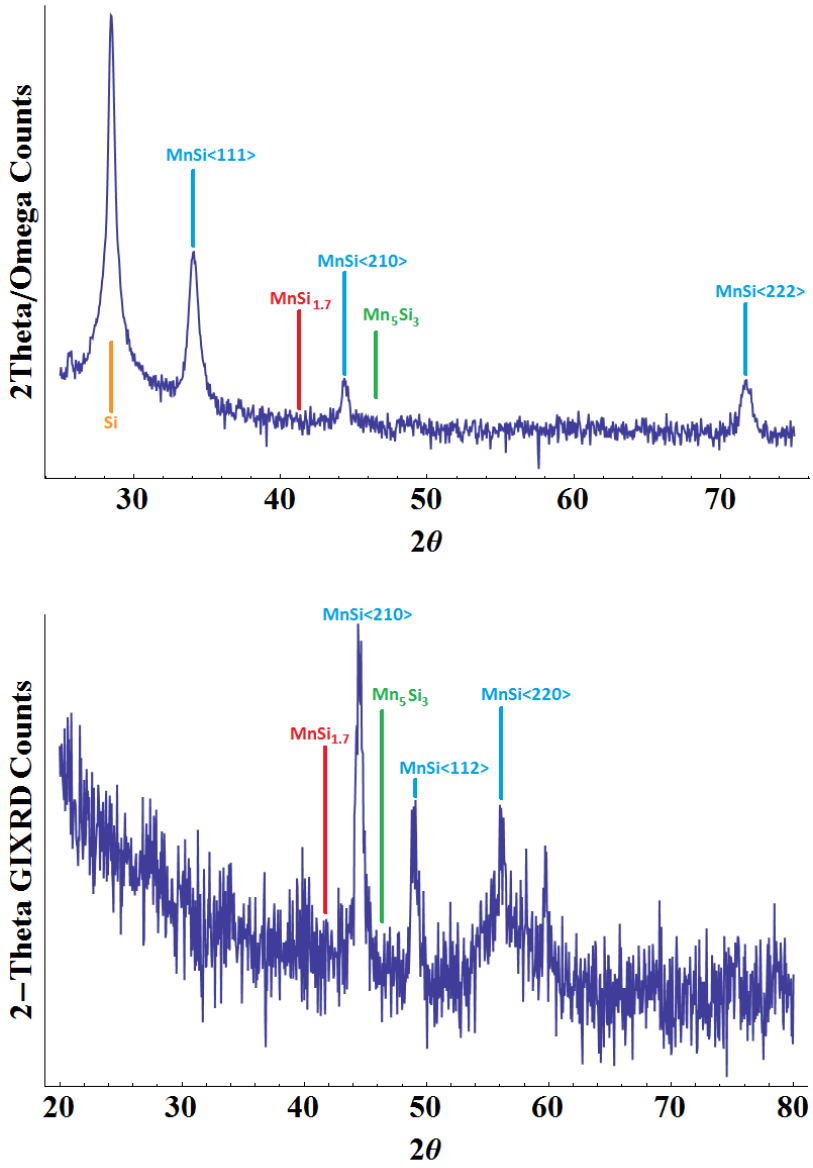

Figure 6.1: MnSi $2\theta/\omega$ and GIXRD 2-θ traces.

still some misalignment of crystallites with respect to the sample plane.

One assessment of film quality was made by taking a rocking-curve measurement about the MnSi peak at 34° to accurately characterize its width (Fig. 6.2). By applying the Scherrer formula

$$w = \frac{K\lambda}{\Delta_{2\theta}} \cdot \cos\theta \tag{6.1}$$

the size of the individual crystallites making up the MnSi film is found to be $15nm$. This is as expected because the film thickness is also $15nm$ and crystal grain dimensions and film thickness are known to be nearly equal in high-quality sputtered films.

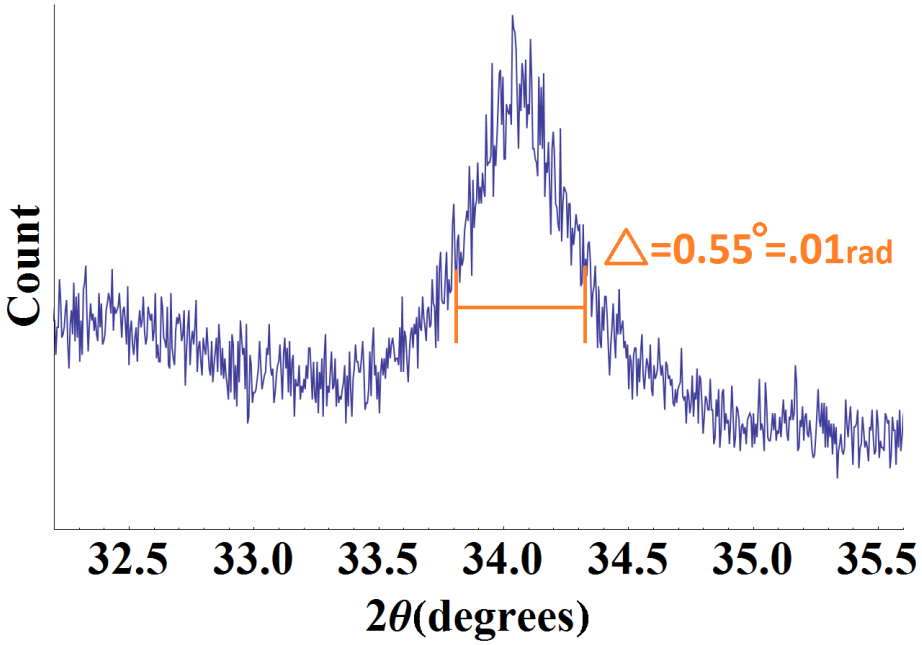

Figure 6.2: Rocking curve for MnSi about the primary peak. The width at half-maximum is .01 radians.

To determine texture of the film a pole figure measurement (see Section 5.3.3) was carried out, again centering on the primary <111> peak. The results are shown in Figure 6.3. The presence of a strong peak in the <111> direction (the north pole for the pole figure sphere) indicates that the normal vector to the grains is highly aligned to that axis (and therefore the substrate Si<111>) throughout the film. The absence of any other peak means that the grains of the film are completely disordered in the plane, each having a random orientation about the <111> axis.

Taken together these measurements indicate that I have successfully deposited a high-

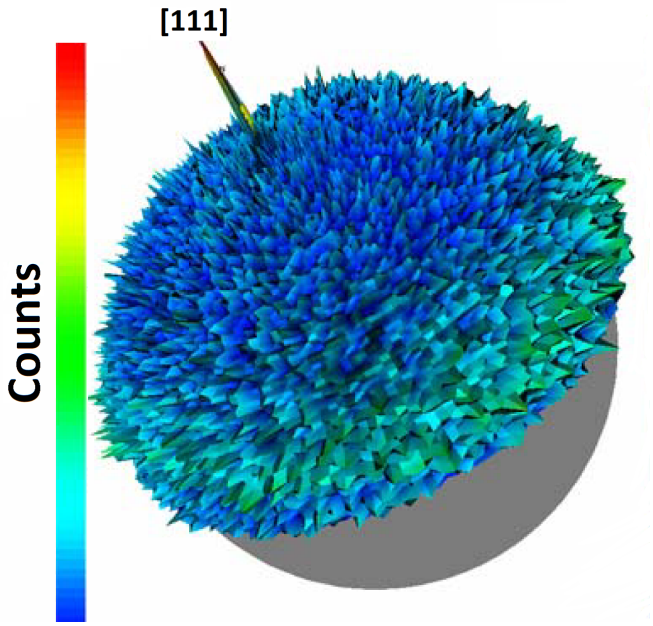

Figure 6.3: MnSi Pole figure centered on the <111> axis.

quality polycrystalline film of B20-phase MnSi by sputtering for the first time. The random orientation of grains in the plane observed in Fig. 6.3 also occurs in MBE-grown films though the grains in those films are larger [65].

6.1.2 MnSi on AlOx

It was found that MnSi grown and annealed on with a thin ∼3nm layer of amorphous aluminum oxide between the MnSi and the Si<111> substrate (prepared as described in Chapter 5) exhibited an XRD spectrum consistent with the presence of pure cubic B20 MnSi. However, the film produced in this way appears to be partly structured parallel to the plane of the film but largely disordered perpendicular to it, as shown by the 2-θ/ω and grazing incidence spectra (Fig. 6.4). The possibility of depositing a thin film chiral ferromagnet, regardless of increased disorder or imperfect orientation on something other than a seed layer with the same structure is a new one, and will add flexibility to studies of skyrmion-hosting materials. In this case, using the AlO_x

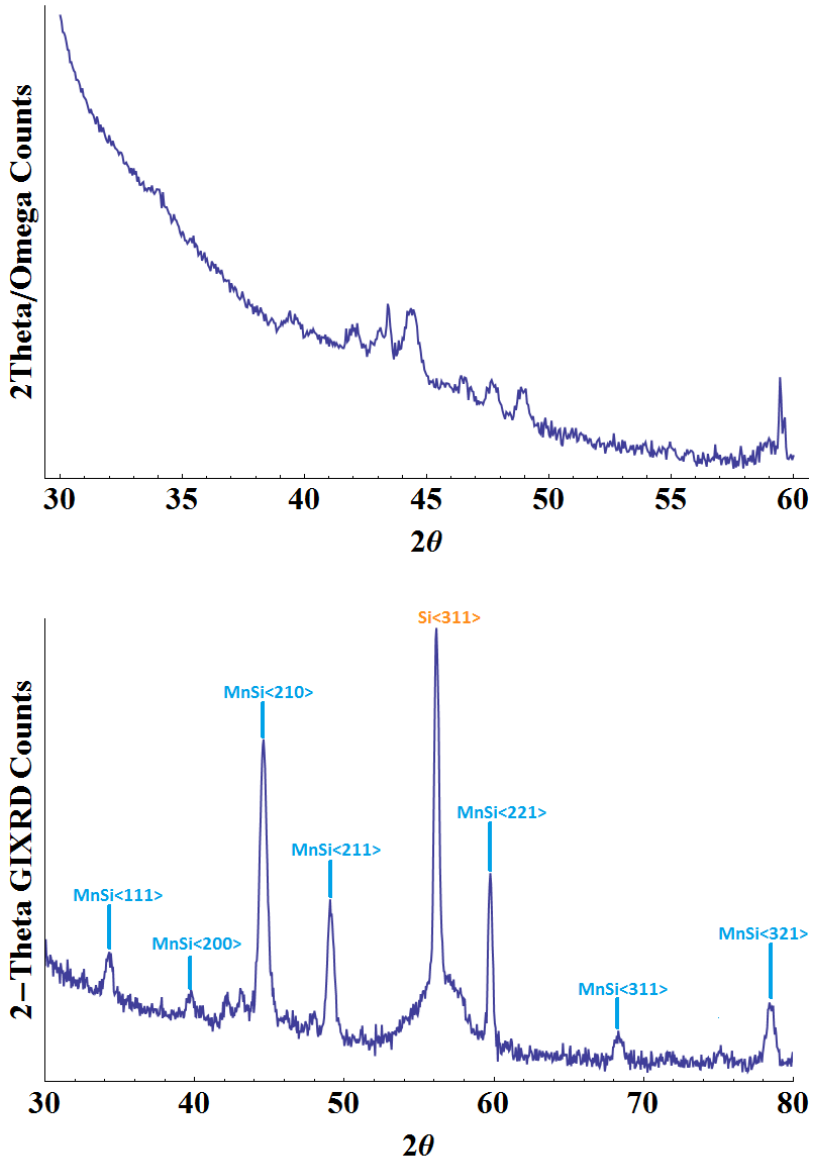

Figure 6.4: MnSi deposited on AlO_x $2\theta/\omega$ and GIXRD 2-θ traces.

protective layer makes it unnecessary to etch the substrate immediately before deposition. In addition, altering the orientation of the MnSi film makes it possible to study other physics, such as controlling the orientation of surface anisotropy contributions with respect to the crystal structure or making it easier to form in-plane skyrmion lattices structures as those studied in [87].

6.1.3 MnSi on Ta

Various attempts were made to deposit MnSi on top of other thin layers that were themselves deposited on etched Si<111>. Deposition on a layer of $5nm$ thick Ta succeeded (via the procedure described in Chapter 5). The resulting XRD spectra (Fig. 6.5) are consistent with the presence of cubic β-Ta and B20 MnSi with an in-plane structure, similar to the result for MnSi deposited on AlO_x. Peaks from the Ta underlayer are observable in the GIXRD spectrum because the layer was relatively thick and the atomic number of tantalum is high.

The possibility of depositing MnSi on relatively thick layers of tantalum is important because it improves the chances of studying the behavior of skyrmions under the influence of spin currents injected by the spin Hall effect [88, 89]. Tantalum has one of the best conversion rates between normal and spin Hall current of all materials [90] and generates spin Hall currents of opposite polarity to platinum so that sandwiching a material between Ta and Pt nearly doubles the amount of spin current that can be injected. The possibility of depositing MnSi between Ta and Pt also opens the possibility of making multilayers with both bulk and interfacial DMI [80](if the MnSi can be made thin enough without contamination). In Section 6.3 below, it is shown that the MnSi deposited on tantalum exhibits signs in its longitudinal magnetoresistance of hosting skyrmions in a narrow temperature range.

6.1.4 FeGe on MnSi

B20 FeGe was deposited on etched MnSi as described in Section 5.2.2. Confirmation of this success was made by a $2\theta/\omega$ XRD scan shown in Figure 6.6. The main competing phase is hexagonal FeGe which is not present. Only FeGe and MnSi contribute to the spectrum and the distinctive <111> peak of cubic FeGe at 2θ =33° is clear.

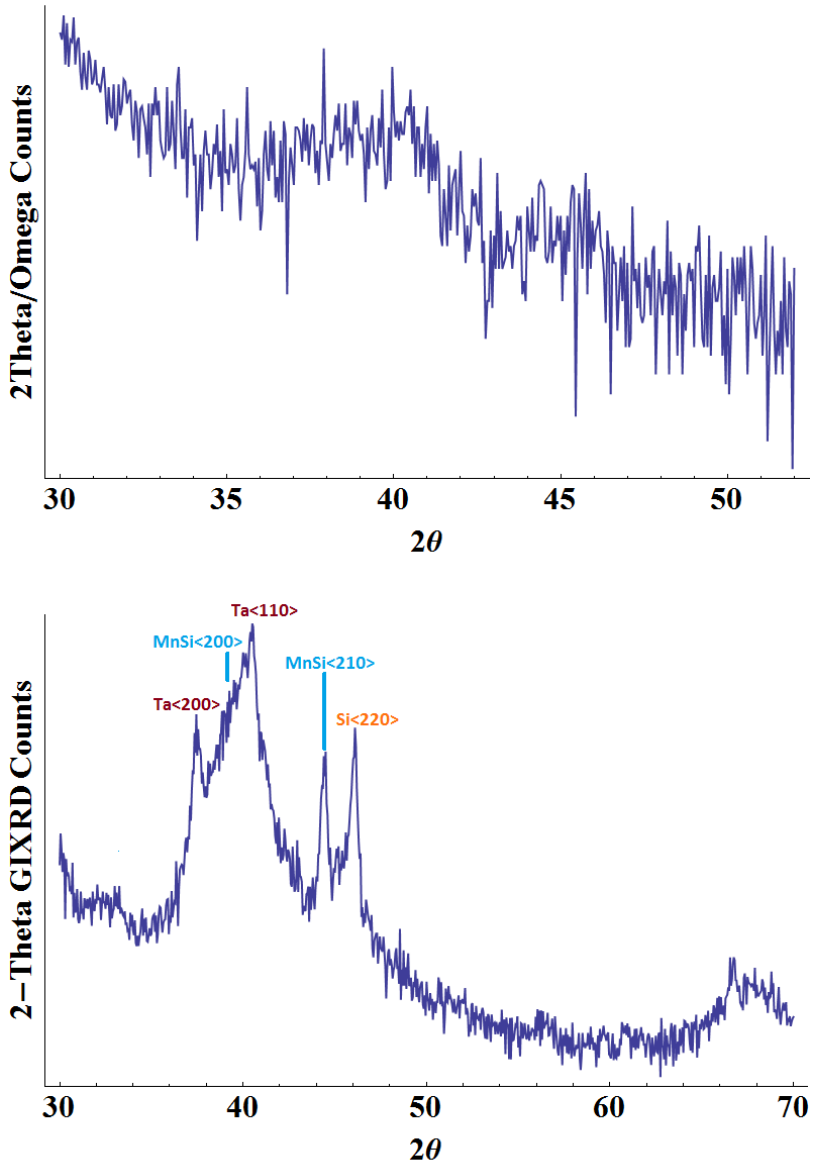

Figure 6.5: MnSi deposited on AlO_x $2\theta/\omega$ and GIXRD 2-θ traces.

The pole figure (Fig. 6.7) for FeGe about the <111> axis differs markedly from that for MnSi, here the signal is concentrated in seven peaks with six surrounding a stronger central peak aligned with <111>. The six peaks are separated from each other by 60° in the in-plane angle β and are 20 degrees above the equator ($\alpha = 20°$ see Fig. 6.7(b)). Since the central peak is present and we know from Fig. 6.6 that there is no hexagonal FeGe present, we can interpret this pole figure as showing a texture

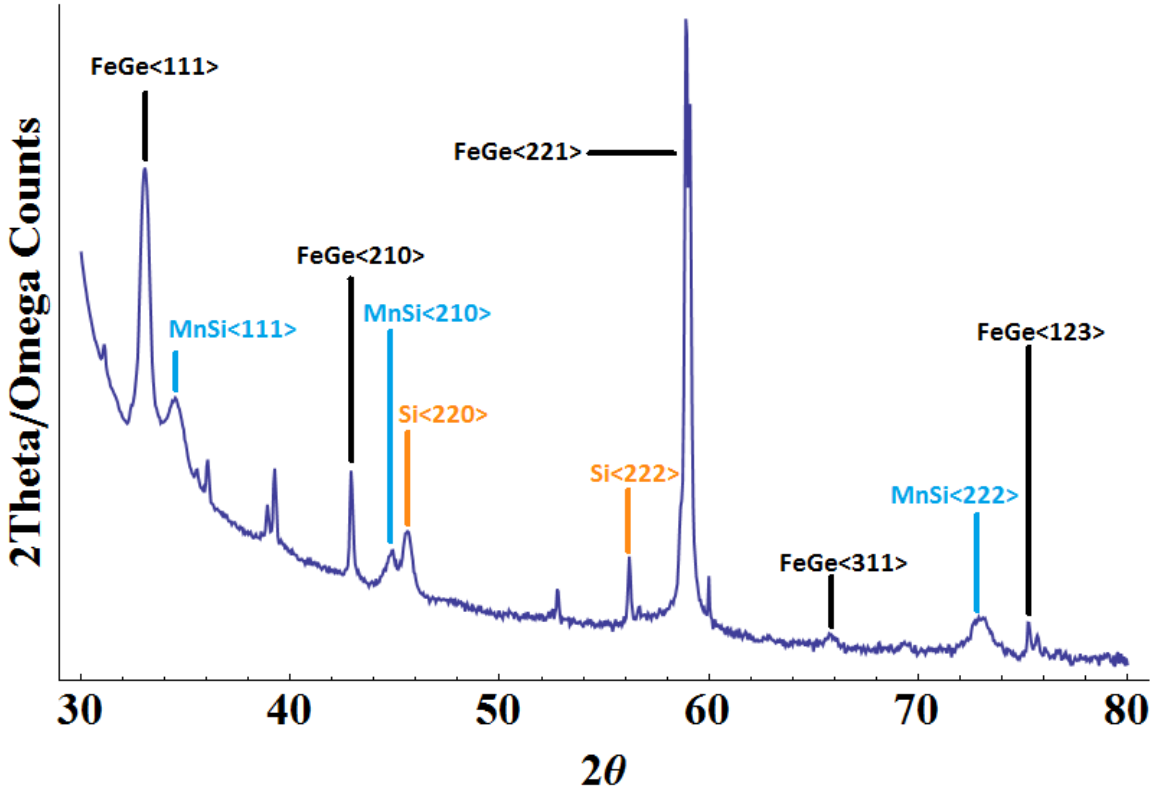

Figure 6.6: FeGe $2\theta/\omega$ XRD spectrum.

consisting of just two opposite (rotated 180° with respect to each other) orientations of grains with cubic crystal structure aligned with its corner (the <111> direction). It is unclear why MnSi has random in-plane orientation while the FeGe grains align in one of only two directions (though there is also three-fold degeneracy for each of these two orientations).

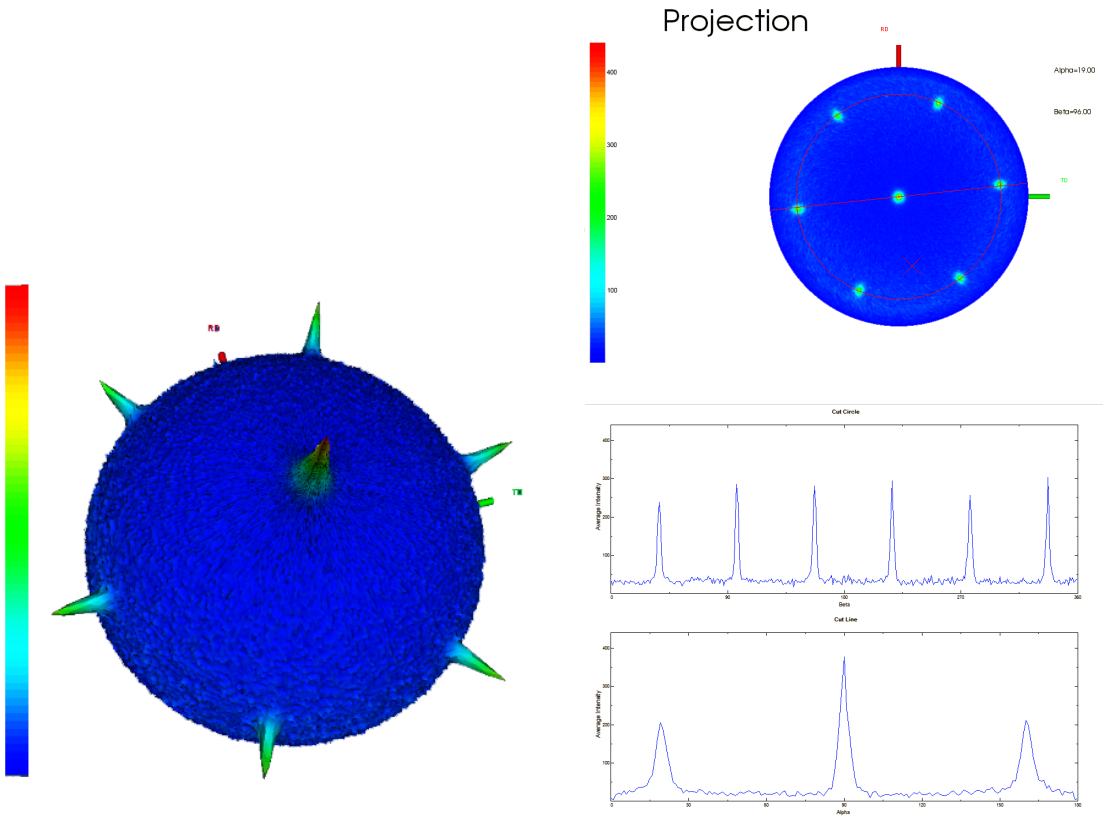

(a) (b)

Figure 6.7: (a) Pole figure for FeGe on MnSi/Si<111>. (b) Projection looking down on <111>.

6.2 Longitudinal Resistivity vs. Temperature

6.2.1 MnSi

The electrical characterization of the sputtered MnSi films begins with the measurement of the longitudinal resistivity ρ_{xx} as a function of temperature. The measurement was made using a Keithley 2400 DC current source and multimeter with a fixed current of 40μA. The source/multimeter was connected to the four-point electrical measurement structure. The results are shown in figure 6.8 with the relevant measurement configuration.

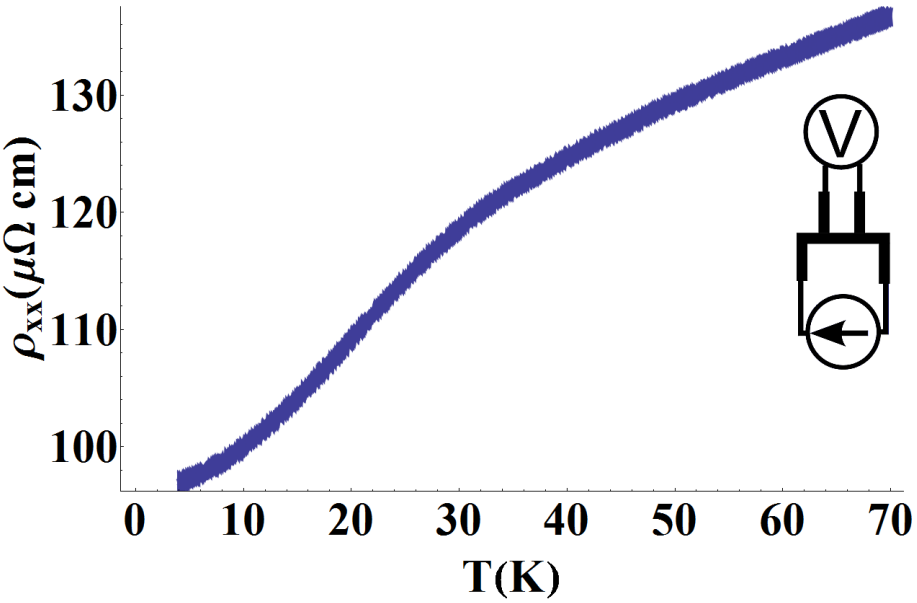

Figure 6.8: MnSi longitudinal resistivity as a function of temperature.

These results are comparable to those obtained for thin films of MnSi grown on Si<111> by molecular beam epitaxy (MBE) [65, 70] as well as single crystals [91, 92], though with indications of somewhat diminished film quality compared to MBE growth. Since the form of the B20 MnSi resistivity versus temperature curve is distinctive, its successful reproduction in the MnSi films grown for this thesis is encouraging.

Ta Underlayer

The presence of a 5nm tantalum underlayer does not significantly alter the shape of the resistivity versus temperature curve, though the magnitude of the resistivity is increased (see Figure 6.9). It is important to note that this large resistivity is not the resistivity of the MnSi alone but rather of the whole Ta[5nm]/MnSi[15nm]/Pt[5nm] multilayer.

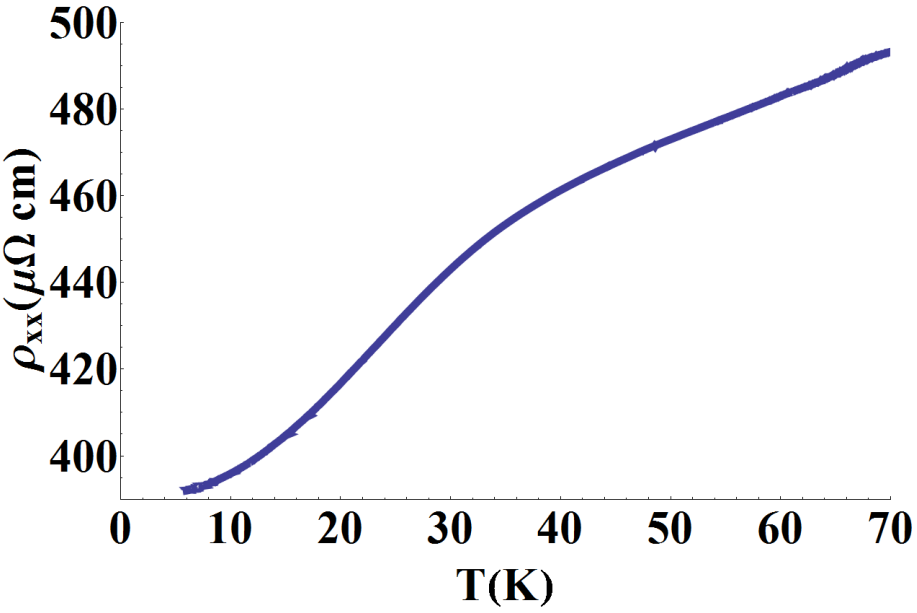

Figure 6.9: 15nm MnSi with a 5nm Ta underlayer on Si<111>: longitudinal resistivity as a function of temperature.

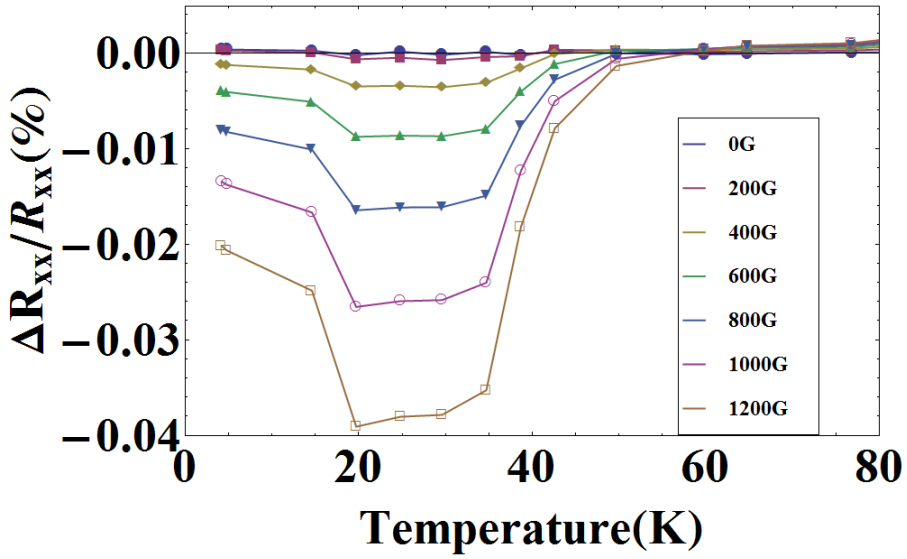

Figure 6.10: MnSi longitudinal magnetoresistance as function of temperature for different out-of-plane applied magnetic fields.

6.3 Longitudinal Magnetoresistance

6.3.1 MnSi

The first indication that the sputtered MnSi films possess a skyrmion-hosting state is obtained from the magnetoresistance of the films and its temperature dependence. As discussed in Chapter 3, this is not typically considered absolute confirmation of the presence of skyrmions because the mechanism by which the skyrmion texture could produce an effect on magnetoresistance does not currently have an accepted explanation. However, a peak in negative magnetoresistance has been found to coincide with the skyrmion state whenever it occurs in a B20 phase chiral magnet.

Magnetoresistance

Figure 6.10 shows the dependence of magnetoresistance on temperature at multiple magnetic fields applied perpendicular to the plane of the film. Here, magnetoresistance is defined as

$$MR(H) = \frac{\rho_{xx}(H) - \rho_{xx}(0)}{\rho_{xx}(0)}. \tag{6.2}$$

The measurements are made on the same kind of thin film structure and measurement arrangement shown in Fig. 6.8. Unlike the zero-field resistivity measurements shown above, these measurements were made using a Keithley 2182A nanovoltmeter and a Yokogawa GS200 as a current source. The current applied was 150μA.

As with the temperature dependence of the longitudinal resistivity, these results are consistent with those obtained for bulk single crystal [91], single crystal nanowire [77], and MBE-grown thin films [70] of MnSi. The magnitude of the magnetoresistance for all thin films is less than for single crystals at the same applied field. Also, the applied fields for the measurements presented here are smaller than those presented in the literature. This may explain the broad minimum in Fig. 6.10 (corresponding to the presence of skyrmions) which is consistent with the slight broadening of the minimum for lower fields observed in the single crystal nanowires of [77] (this field was still four times as high as the highest field shown in Fig. 6.10) but not in the bulk single crystals of [91].

Below the temperature that we propose corresponds to the initial presence of skyrmions ($\sim$20K), the MnSi is in a conical state (shown in Chapter 4) where the magnetoresistance depends on the magnetic field applied. Above the critical temperature ($\sim$50K) the MnSi film is in a paramagnetic state so that the magnetoresistance is zero and unchanged with applied field strength.

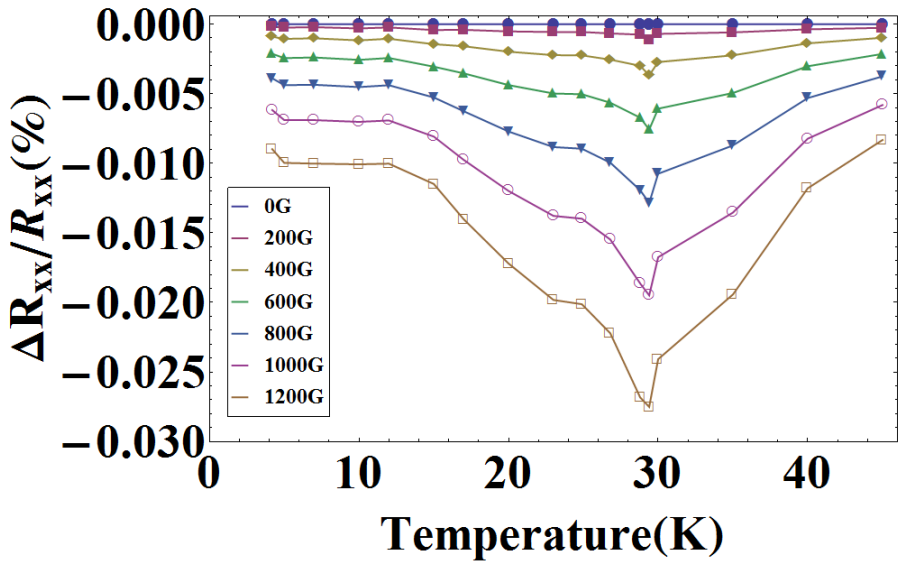

Figure 6.11: MnSi longitudinal magnetoresistance in the presence of a 5nm tantalum underlayer as function of temperature for different out-of-plane applied magnetic fields.

Ta Underlayer

When there is a 5nm underlayer of Ta between the Si<111> substrate and the MnSi, the temperature dependence of the magnetoresistance of the MnSi film (see Fig. 6.11) is more like that of a single crystal [92] than MBE-grown films. It exhibits a narrow minimum at the bulk Curie temperature of 29.5K (consistent with the observation that this minimum approaches the bulk transition temperature as the applied field is decreased in [92]) rather than the broad minimum of the film sputter deposited directly on silicon.

6.4 Hall Effect Measurements: MnSi

The standard electrical transport measurement used to confirm the presence of skyrmions is the extraction of a topological component from the Hall resistivity ρ_{xy}. The forms

and origins of the contributions to the ρ_{xy} are discussed in Chapter 3. Here we recall that the Hall resistivity can be expressed as

$$\rho_{xy} = R_0 H + S_H \rho_{xx}^2 M + \rho_{xy}^t \tag{6.3}$$

R_0 is the ordinary Hall resistance, S_H is a magnetic field independent anomalous Hall coefficient, and the magnetization M is itself dependent on applied field H and temperature T. S_H is negative for MnSi so that for low fields the total Hall resistivity is negative. We use the convention of [71, 76] and plot $-\rho_{xy}$ and its derivatives and scalings.

The measurements described below were carried out on a Hall cross of the type shown in Chapter 5 with a width of 1μm and an arm length of 5μm. All measurements were carried out in a ^4He immersion cryostat.

6.4.1 Low Current Density

These measurements were taken using a resistance bridge and lock-in technique. The lock-in amplifier (A Signal Recovery DSP 7265) was set up in FET mode with 60Hz and 120Hz line rejection filtering and the lock-in frequency was 2333 Hz. The AC voltage amplitude applied to the Hall cross corresponded to an applied current of 1μA. Measurement was on the transverse arms.

In the low field (0G - 2kG) regime accessible for this set of measurements the resistivity versus field data taken at multiple temperatures are well fit by a model with linear magnetic field dependence. Figure 6.12 shows the dependence of ρ_{xy} on temperature.

In order to extract the topological term we first use high-temperature (T>60K) data to remove the ordinary Hall contribution. At these temperatures the magnetization

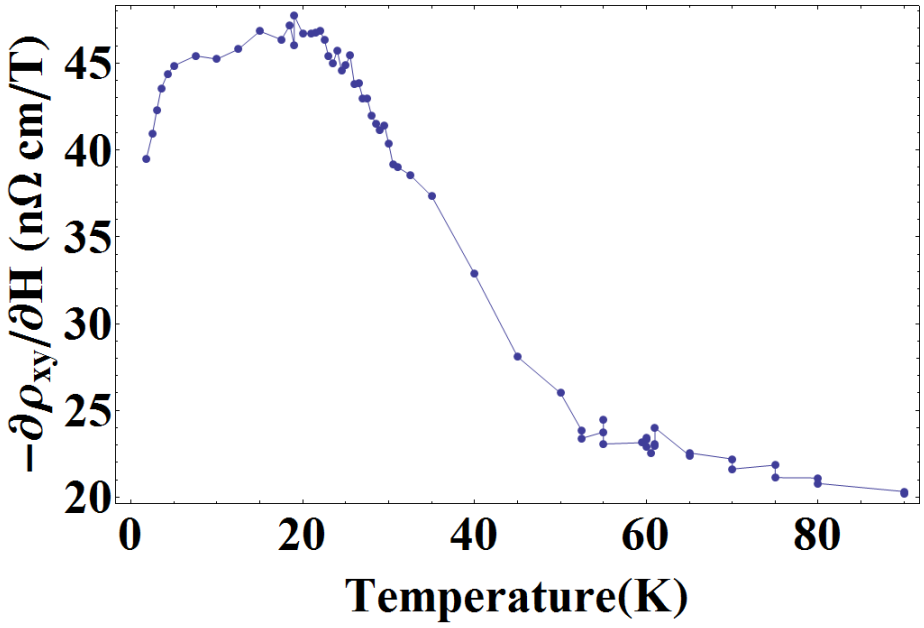

Figure 6.12: Linear coefficient for the fit of Hall resistivity as a function of applied magnetic field plotted against temperature.

of MnSi is zero and there are no skyrmions. Therefore the remaining contribution to $\partial\rho_{xy}/\partial H$ (which is linear in T) is attributed to R_0 and is subtracted at all temperatures. The high-temperature data and fit are shown in Figure 6.13.

Next, the resulting data are divided by ρ_{xx}^2 at the corresponding temperature (see Fig. 6.8) and the T dependence of M (which for MnSi is linear in H in this field range [65]) is approximated by fitting to

$$b_1(1-\frac{T}{2T_0})^{b_2 f(T)} \tag{6.4}$$

Where

$$f(T) = C\frac{\coth(C/(1-a(T))}{\sinh(C/(1-a(T))}\frac{a(T)}{(1-a(T))^2} \tag{6.5}$$

with the constant $C = \frac{1}{2}ln(\cot(\pi/8))$ and $a(T) = (1-T/(2T_0))$. $f(T)$ is the effective critical exponent of the magnetization for the exact solution to a finite 2-dimensional

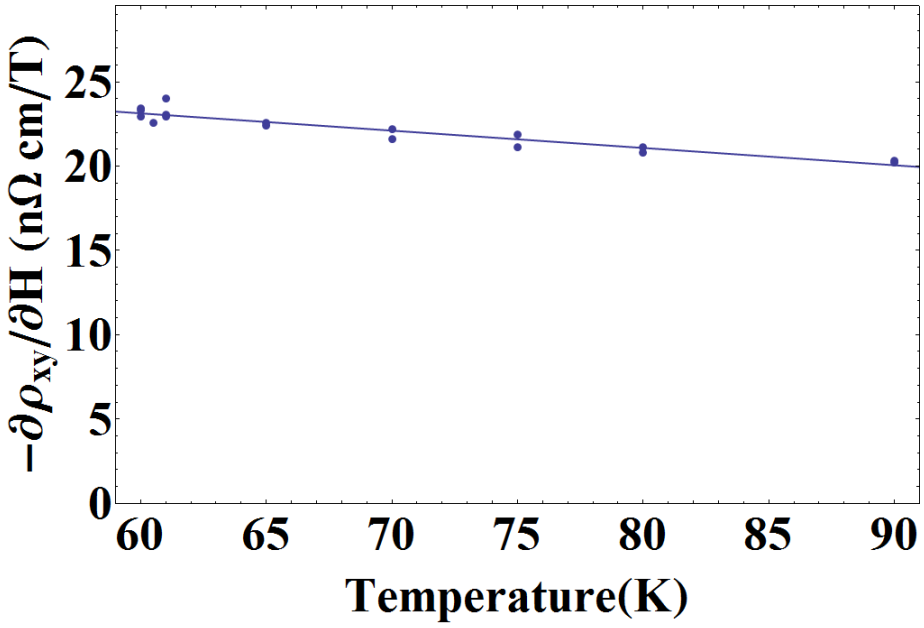

Figure 6.13: High temperature ρ_{xy} and least-squares fit linear in temperature.

Ising model [93]. There are 3 parameters, b_1 is fixed by the low-temperature value of $\partial\rho_{xy}/\partial H$ (where ρ^t_{xy} should be zero). T_0 is set by the temperature at which $\left(\partial\rho_{xy}/\partial H - R_0(T)\right)/\rho^2_{xx}$ goes to zero. The parameter b_2 captures some features corresponding to the finite thickness of the sample, but could be set to one and reasonable values of ρ^t_{xy} would still be obtained. However, this would give an unphysically steep decrease in M as a function of temperature so this single parameter is allowed to vary to obtain a least squares fit to the data. The results of this fit are shown in Fig. 6.14. The fit for the anomalous Hall contribution could be improved by further taking into account the finite thickness of the MnSi film either via a mean-field or quantum Monte Carlo calculation of the magnetization [94, 95] so that the nonzero slope of the magnetization at low temperatures [65, 92] is better reproduced. However the improvement is likely to be incremental and a better strategy would be to measure the magnetization directly and fit for the single constant S_H. The likely result is that the magnitude of the topological term would be slightly decreased and

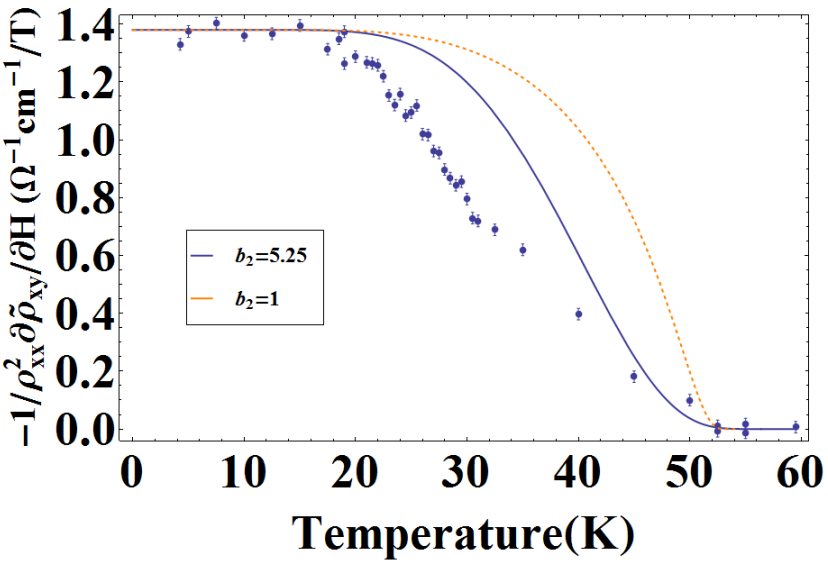

Figure 6.14: Reduced Hall resistivity data and fits for $S_H M/H$ plotted against temperature. $\tilde{\rho}_{xy} = \rho_{xy}^{AHE} + \rho_{xy}^{t}$ so that the curves are approximations to $S_H M/H$ (M is linear in H in this field range). The difference between the fit and the observed data is ρ_{xy}^{t} (plotted in Fig. 6.15). See text for the meaning of b_2.

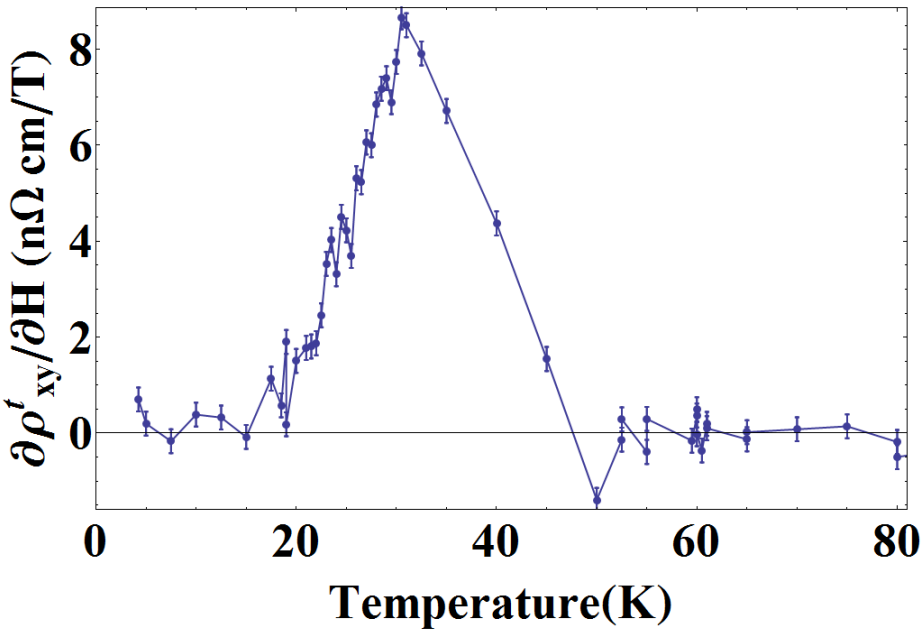

Figure 6.15: Topological component of the magnetic field derivative of the Hall resistivity. Multiplying by a low field gives the topological Hall resistivity at that field.

the temperature range over which it is non-zero would be slightly narrowed.

Subtracting the anomalous Hall contribution found in this way and multiplying the remainder by ρ_{xx}^2 (and removing the sign that we have been carrying until now) gives the result for $\partial\rho_{xy}^t/\partial H$ plotted in figure 6.15. Since ρ_{xy}^t is nearly linear in this field range (up to approximately 5kG) this result is sufficient for comparison to existing results for MBE-grown thin-film [65] samples with which agreement both in terms of temperature range and magnitude of the topological signal is very good. As with the MBE films, the temperature range over which the topological Hall effect is present is broadened in comparison to single crystals of MnSi [71]. This is the primary experimental result of this work: sputtered MnSi films are comparable to MBE-grown films in their ability to host skyrmions.

In addition, the temperature range in which we observe a finite topological Hall effect

(and therefore skyrmions) agrees completely with the minimum in the longitudinal magnetoresistance discussed above. This is therefore another case where the presence of skyrmions suggested by a magnetoresistance measurement is confirmed by a different measurement.

Chapter 7

Approximation of Skyrmions

7.1 sine-Gordon Kinks

Recall the Euler-Lagrange equation for the azimuthal angle of the local magnetization in an isotropic ferromagnet with a Dzyaloshinkii-Moriya interaction (Eq. (2.31)) from Chapter 2:

$$\theta_{\rho\rho} + \frac{1}{\rho}\theta_\rho - \frac{1}{2\rho^2}\sin 2\theta = \frac{h}{2}\sin\theta + \frac{d}{\rho}\sin^2\theta \tag{7.1}$$

If rather than setting the entire right hand side to zero, as in Section 2.5, we consider a case with the Dzyaloshinskii-Moriya coefficient $D = 0$ in Eq. (2.31) we have

$$\theta_{\rho\rho} + \frac{1}{\rho}\theta_\rho = \frac{1}{2\rho^2}\sin 2\theta + \frac{h}{2}\sin\theta \tag{7.2}$$

This equation is a circularly symmetric double sine-Gordon equation [96, 97] with a variable coefficient on the $\sin 2\theta$ term. Unfortunately, there is no known analytical solution for this equation either. So we have to fall back to the one-dimensional,

stationary sine-Gordon equation [98, 99]

$$\theta_{xx} = \sin\theta(x) \tag{7.3}$$

This equation admits an exact soliton solution known as a sine-Gordon kink:

$$\theta(x) = 4\arctan(e^{-x}) \tag{7.4}$$

Eq. (7.4) for the 2π-soliton is equal to double the Bloch domain wall magnetization profile $\theta_{DW}(x) = \arccos(\tanh(x))$ derived by Landau and Lifshitz [100, 84]. This is to be expected because the static Landau-Lifshitz model (with magnetization constrained to an "easy" plane) is a static sine-Gordon equation with $\frac{1}{2}\sin 2\theta$ on the right-hand side. The mathematics of the sine-Gordon kink soliton has long been used in the study of domain wall properties, stability, and dynamics in one-dimensional ferromagnetic chains [101, 102] and easy-plane ferromagnets [103, 104, 105] because of this correspondence [60].

7.2 Kink Approximation in Two Dimensions

The kink solution Eq. (7.4) has an interesting relationship to the skyrmion profile. Skyrme himself [106] used the sine-Gordon model as precursor and toy version of his model and was the first to discover the two-soliton sine-Gordon solution. Some time ago Sutcliffe found [107] that the kink (suitably scaled for size) provides an excellent approximation to the radial profile of a three-dimensional skyrmion. More recently, Nitta showed [108] that a two-dimensional skyrmion is topologically equivalent to a sine-Gordon kink inside (superimposed on a background of) a domain wall.

It turns out that the $x > 0$ half of the sine-Gordon kink soliton is also a very good

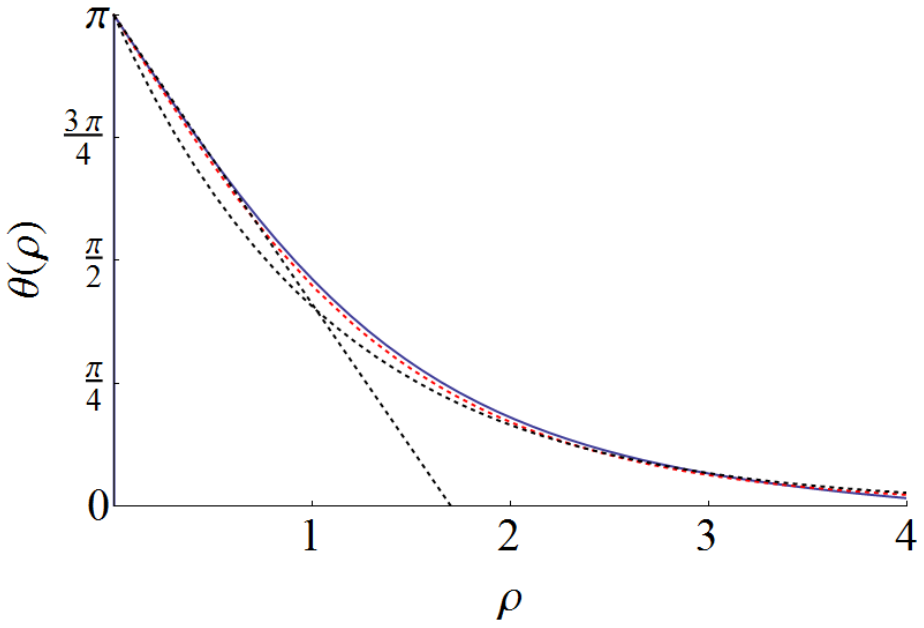

Figure 7.1: A numerical solution for a skyrmion profile (blue) with its corresponding sine-Gordon kink approximation Eq. (7.5)(dashed red). Linear and exponential approximations are shown as dashed black curves.

approximation to the profile function of the two-dimensional skyrmion for the case of high magnetic fields (relative to the DMI constant). In Figure 7.1 I show the close match between a kink approximation

$$\theta(\rho) = 4\arctan(e^{-\rho/\delta}) \tag{7.5}$$

where δ is the width or size of the kink, and the solution of Eq. (7.1) obtained numerically by the shooting method in figure 7.1. In this case δ was used as a fitting parameter. This fact has not been reported previously in the literature. However, this approximation fails badly for intermediate and low applied magnetic fields.

7.3 Two-Parameter Approximations

A two-parameter generalization of the sine-Gordon kink

$$\theta(x) = 2\arctan\left(\frac{a}{c_1 \sinh x/c_2}\right) \tag{7.6}$$

exactly solves a *linear* double sine-Gordon equation with *constant* coefficients [97]

$$\theta_{xx} = \frac{1}{2}\left(\frac{1}{c_1^2} - \frac{1}{c_2^2}\right)\sin 2\theta + \frac{1}{c_1^2}\sin\theta \tag{7.7}$$

Note that Eq. (7.6) and Eq. (7.4) are equal if $c_1 = c_2 = 1$. Various forms of this solution have been used to study domain walls on 1D ferromagnetic chains with anisotropy [109]. Particularly relevant to our study of Eq. (7.1) is the discovery of a static soliton solution for the case of an isotropic ferromagnetic chain [110, 60] and its explanation [111] as an "untwisted" (achiral) or "twisted" (chiral) bound pair of two π-Bloch domain walls separated by a distance $2\tilde{R}$:

$$\theta(x) = 2\arctan e^{-\frac{x}{\delta}-\tilde{R}} + 2\arctan e^{-\frac{x}{\delta}+\tilde{R}} \tag{7.8}$$

The like sign on x for the two domain walls indicates that they have the same sense of twist (same chirality) defined by

$$\tau = \frac{1}{2\pi}\int_{-\infty}^{\infty} dx \frac{df(x)}{dx} \tag{7.9}$$

where $f(x)$ may be either member of the pair or their combination, so that the pair is chiral with $\tau = 1$. The combination Eq. (7.8) can be rewritten as

$$\theta(x) = 2\arctan\left(\frac{\cosh\tilde{R}}{\sinh(x/\delta)}\right) \tag{7.10}$$

Where $\tilde{R}$ is still half the separation between the domain walls and δ is their width. Such a bound pair of two solitons, in this case Bloch walls, is often known as a "bion" [60] and is itself a soliton. The 1D structure so defined is shown in Figure 7.2.

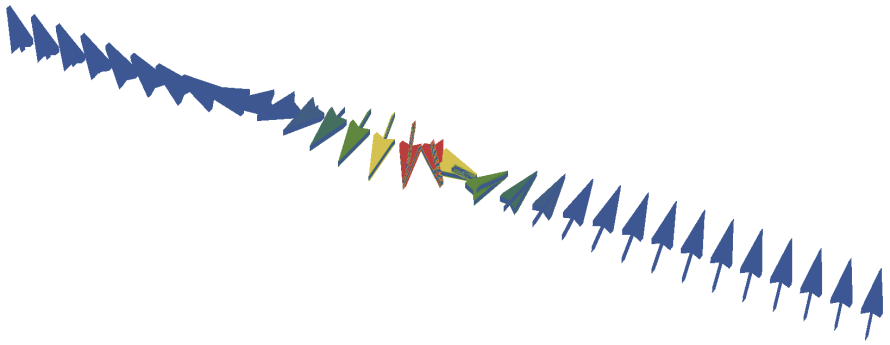

Figure 7.2: The pair of π domain walls described by Eq. (7.10).

The approximation approach proposed here is to replace x in the twisted Bloch wall pair discussed above with ρ to describe the radial profile of the (rotationally symmetric) approximate two-dimensional skyrmion. This sort of approximation has been used previously for two-dimensional (vortex) solitons of the dissipative cubic complex Ginzburg-Landau model of a laser [112] but not in the context of skyrmions, though it is standard to define skyrmions in three and higher dimensions in terms of their profile function as is done here.

Though the approximation given by Eq. (7.10) as a function of ρ can be used to successfully fit numerical solutions for the skyrmion profile via the parameters $R = \cosh\tilde{R}$ and δ, it is more useful to be able to predict the skyrmion profile using the physical parameters h and d (the reduced magnetic field and Dzyaloshinskii constant respectively of Section 2.5). To that end we solve Eq. (7.1) numerically using a shooting method in the Mathematica analysis software package for several combinations of h and d values (see Appendix A for the code listing and details). One important

feature of solutions to Eq. (2.31) is that h and d must have opposite signs. In this thesis I take $h > 0$ (corresponding to $\theta(0) = +\pi$) which implies that $d < 0$, all future references to d are shorthand for $|d|$ unless otherwise specified. Values of R and δ which give the best least squares fits for these profiles were found and used to extract phenomenological forms for R and δ in terms of h and d. The resulting expressions are

$$R = 2.5\left(d\sqrt{\frac{1}{d^2}+\frac{1}{h}}-1\right) \tag{7.11}$$

$$1/\delta = 0.346 + 1.9\left(1-\frac{1}{h\sqrt{\frac{1}{d}+\frac{1}{h^2}}}\right) \tag{7.12}$$

Figure 7.3 shows the degree to which the phenomenological expressions match the numerical results for R and δ.

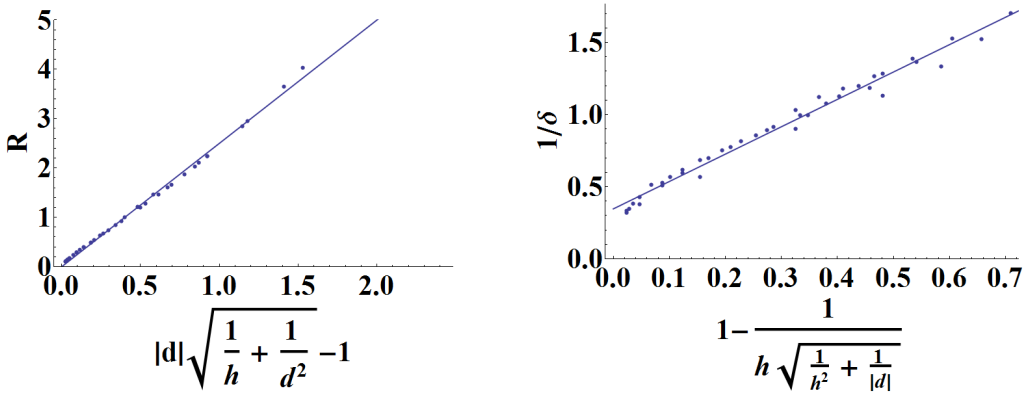

(a) (b)

Figure 7.3: (a) Relation between the parameter R and the physical parameters h and d, the slope of the line is 2.5. (b) Relation between $1/\delta$ and h and d, the line is given by 0.346 + 1.9f(h,d).

The success of this approximation is shown in Figure 7.4 where the approximation is shown to be close to the numerical solution over a relatively wide range of ratios of h to d. The figure is designed for easy comparison to Figure 2(c) of [56]. None of the

h and d combinations were used to find Eq. (7.11). The approximations were made using only the value of h/d and do not have any fitting parameters. One limitation of this approximation is that it does not work for large values of $h/d > 2$, however single skyrmions are not considered stable for $h/d > 1.6$ [16].

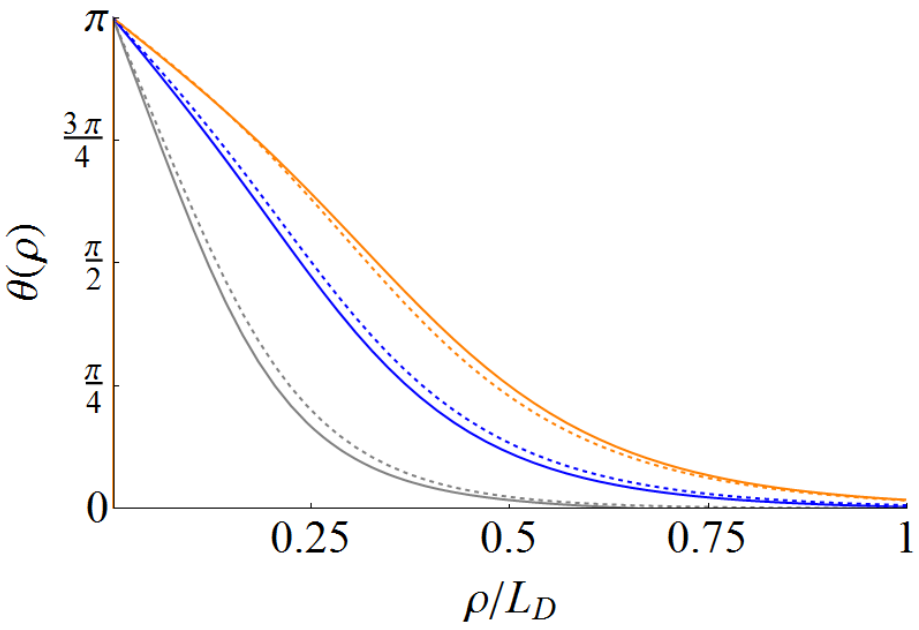

Figure 7.4: Numerical shooting method (solid) and approximation Eq. (7.10) and Eq. (7.11) with $x \to \rho$ (dashed) skyrmion profiles with gray, blue, and orange corresponding to $\mathrm{HA/D^2} = 1.4$, 0.8, and 0.6

For comparison to other available analytical approximations for 2D skyrmions, in Fig. 7.5 we show the best possible fit of the approximation Eq. (2.34) from [59] with two free fitting parameters for one of the cases shown in Fig. 7.4. This is the only current single approximation which correctly matches the skyrmion profile at both $\rho = 0$ and $\rho = \infty$ but the approximation presented in this thesis performs better for single skyrmions over the whole profile.

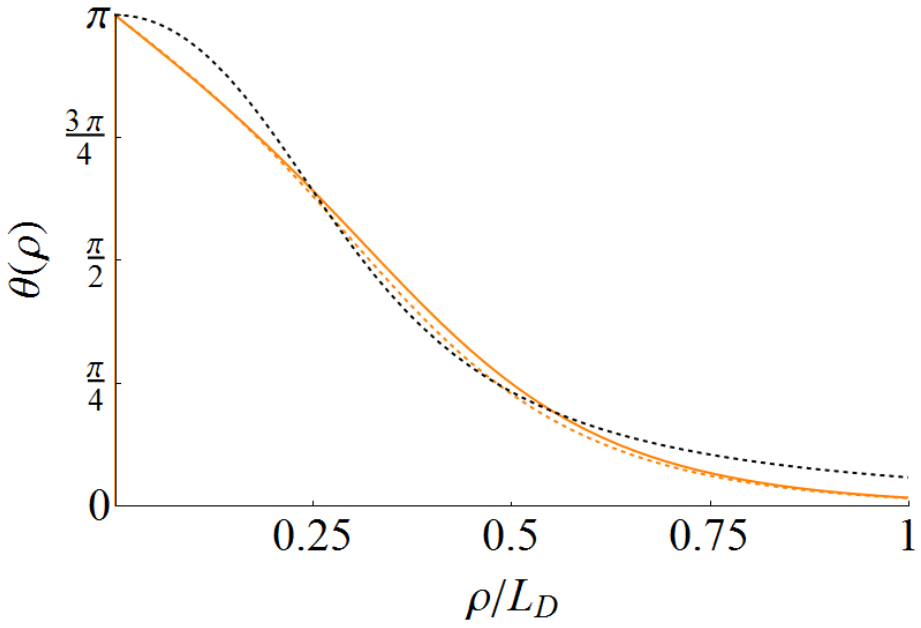

Figure 7.5: Numerical shooting method (solid) and approximation Eq. (7.10) and Eq. (7.11) with $x \to \rho$ (dashed orange) corresponding to $\mathrm{HA/D^2} = 0.6$ as in Fig. 7.4. For comparison (dashed black) shows the best fit of approximation Eq. (2.34) to the numerical solution with both parameters (R and p) allowed to vary without restriction.

7.3.1 Approximate Energy Calculation

The utility of such an approximation is that it can allow the calculation of features of skyrmion structure and dynamics in micromagnetic calculations [26] without requiring calculation of or "relaxation" into the initial skyrmion structure under the specific conditions of interest. In order to go further and use the approximation to determine the stability and features of skyrmions for different values of applied magnetic field and the material dependent strength of the Dzyaloshinskii-Moriya interaction it is necessary to calculate the energy of the approximate skyrmion. This is accomplished by integrating the energy density mentioned in Section 2.5 and reproduced here:

$$w = 2\pi AM^2 \left[\left(\theta_\rho^2 + \frac{\sin^2\theta}{\rho^2} \right) + d\left(\theta_\rho + \frac{\sin 2\theta}{2\rho} \right) + h(1-\cos\theta) \right] \rho \qquad (7.13)$$

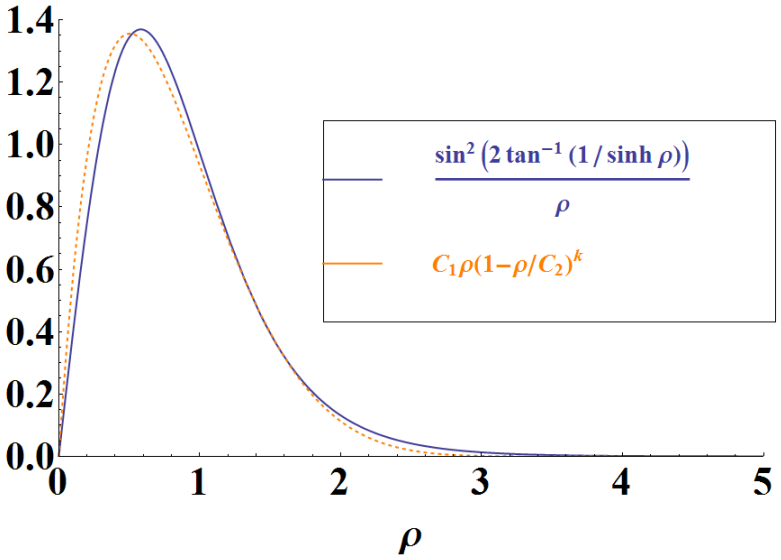

Figure 7.6: (blue) The second term of the energy density Eq. (7.13) (ignoring constant prefactors) with R and δ both set to one. (orange) The approximation described in the text with C_1=6.83,C_2=4,and $k = 6.957$.

The integration is over the variable ρ and for a single skyrmion the integration limits are from zero to infinity. For $\theta(\rho)$ given by Eq. (7.10) with $x \to \rho$, all terms with the exception of the second can be integrated analytically using the symbolic computation package Mathematica, though most of the resulting expressions are long and are collected in Appendix B. The second term requires special consideration because despite appearing innocuous and approaching zero smoothly both at zero and infinity, the integral of

$$\frac{\sin^2\left(\arctan\left(\frac{R}{\sinh(\rho/\delta)}\right)\right)}{\rho} \tag{7.14}$$

plotted in Fig. 7.6 could not be found symbolically.

Fortunately, it is possible to approximate this integrand with an expression of the form

$$C_1\rho(1-\rho/C_2)^k \tag{7.15}$$

Which integrates to

$$\int C_1\rho(1-\rho/C_2)^k d\rho = \frac{C_1(\rho-C_2)(1-(\rho/C_2))^k(C_2+\rho+k\rho)}{(1+k)(2+k)} + \text{const.} \qquad (7.16)$$

This approximation is only real-valued up to $\rho = C_2$ so that C_2 must now be used as the upper limit of integration (or put another way the approximation is defined piecewise so that it is zero for $\rho > C_2$), giving

$$\int_0^{C_2} C_1\rho(1-\rho/C_2)^k d\rho = \frac{C_1 C_2^2}{2+k+k^2} \qquad (7.17)$$

The values of C_1,C_2, and k are determined by R and δ (and therefore indirectly by h and d) and a method similar to the one used above to find a phenomenological approximation for the skyrmion profile function can be applied to complete an analytical approximation for the energy of the (approximate) skyrmion. As a particular example the best least squares fit for ρ=1, R=1 is given by C_1=6.83,C_2=4,and k=6.957 (and shown in Fig. 7.6) and for this case the integral of the approximation differs from the numerically calculated integral of Eq. (7.14) by less than 0.5%.

This analytical expression for the energy allows the possibility of a continuous phase diagram for a single approximate skyrmion as well as the possibility of including additional skyrmions or defects and boundaries to the system and calculating the dependence of the energy on (e.g.) the separation between skyrmions analytically. The latter would allow an analytical approximation for the force between skyrmions to be obtained by taking a derivative.

7.3.2 Approximate Skyrmion Lattice

An interesting feature of the approximation of a skyrmion by a pair of domain walls is that rather than the implicitly circularly symmetric construction obtained by simply replacing the one-dimensional variable x with the radial coordinate ρ (akin to revolving the domain wall pair about its center), we can instead add three or more domain wall solitons in the plane equally spaced in the angular coordinate ϕ. The expression for such a sum with n $(2\pi/n)$-domain walls is given by

$$\sum_{k=1}^{n} \frac{4}{n} \arctan\left((e^{-r/\delta + R\left(r\cos\left(\frac{2k\pi}{n}\right)\cos\phi + r\sin\left(\frac{2k\pi}{n}\right)\sin\phi\right)}\right) \tag{7.18}$$

The symmetry is broken on the R term in the exponential so this is not exactly equivalent to the circularly symmetric approximation discussed above and becomes physically unreasonable for large R (resembling the Belavin-Polyakov soliton discussed in Section 2.5). However, the multi-solitons constructed in this way *are* circularly symmetric for sufficiently small R and δ and even give a better fit to numerical skyrmion solutions under conditions corresponding to high applied fields h.

The case n =6 is of particular interest because it corresponds to an intersection of three of the twisted domain wall pairs discussed above, each pair separated from the next by 120°, and possesses hexagonal symmetry as the skyrmion lattice does. This speaks to an important apparent paradox about the nature of skyrmions. It has been known since the initial observations of skyrmion lattices [12] that they are well described by a "triple-Q" magnetization configuration given by

$$\vec{M}(\vec{r}) \approx M_b + \sum_{i=1}^{3} \vec{M}_{Qi}(\vec{r} + \delta\vec{r}_i) \tag{7.19}$$

with

$$\vec{M}_{Qi}(\vec{r}) = M_{Qi}\left[\vec{n}_{i1}\cos(\vec{Q}_i\cdot\vec{r}) + \vec{n}_{i2}\sin(\vec{Q}_i\cdot\vec{r})\right] \tag{7.20}$$

This expression describes the intersection of three infinite magnetic helices, with amplitudes M_{Qi} and relative shifts $\delta\vec{r}_i$, superimposed on a uniform (out-of-plane) background $\vec{M}_b$. The triple-Q nature of the skyrmion lattice in FeGe has been confirmed by direct observation with Lorentz TEM [67] where skyrmions coexisting with and arising from helical domain walls were studied. However, it has also been known since the first real-space observations of skyrmions [15] that they can exist singly on a uniform ferromagnetic background, which is inconsistent with any requirement for the presence of (semi-)infinite magnetization helices.

The n =6 version of Eq. (7.18) may provide a bridge between descriptions of a single skyrmion and a skyrmion in a lattice since it is an intersection of three chiral helical magnetization structures but with a decay which ensures that like the circularly symmetric approximation it can be described as a single isolated particle, out of which a hexagonal lattice can be built. Also, for higher fields (regimes where skyrmion crystal lattices are stable) the n =6 approximation provides a superior fit to numerical solutions of the skyrmion profile equation when compared to the circularly symmetric approximation (See Fig. (7.7)). However, this is not unique, as other values of n >2 also provide a superior fit in this range and so it is important to emphasize that this is only an approximation and does not perfectly describe the structure of a skyrmion. It is possible that the model with n =3 is more consistent with the results of [67] but may be more difficult to reconcile with the picture of an isolated skyrmion. This may not be a problem because the coexistence of skyrmions and helical domain walls vs. skyrmions and a uniform ferromagnetic background occurs in different regions of magnetic field - temperature phase space [15].

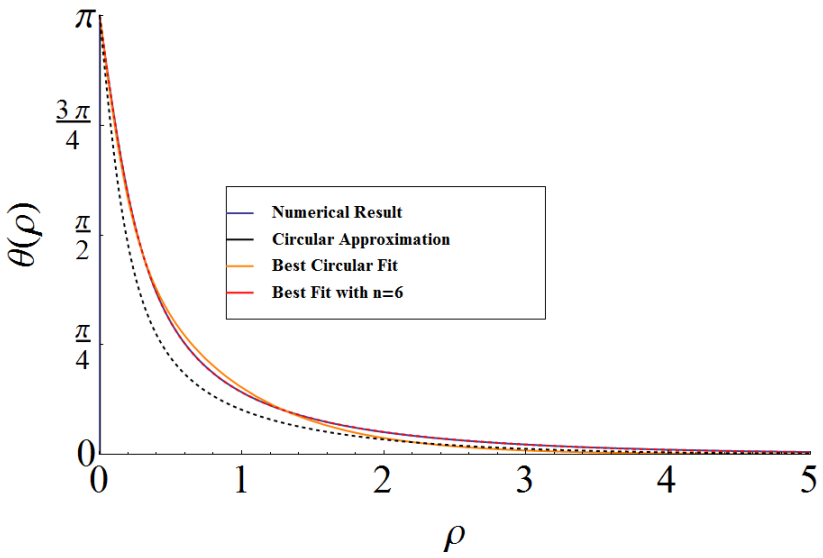

Figure 7.7: Numerical shooting method (solid blue), circular approximation Eq. (7.10) and Eq. (7.11) with $x \to \rho$ (dashed black), best fit for Eq. (7.10), and best fit for Eq. (7.18) with n =6, skyrmion profiles for h=0.6,d=-0.3 ($\mathrm{HA/D^2} = 6.7$).

Chapter 8

Conclusions

8.1 Summary of Results

The main results of this work were the following:

- Deposition of B20 cubic MnSi thin films by magnetron sputtering, both directly on Si<111> (which is a first for sputtering, all previous films being grown by MBE) and with a 3nm AlO_x or 5nm Ta underlayer between Si<111> and MnSi (the first time anything other than a few monolayer seed layer was deposited between).

- Determination that the electrical transport behavior of these films is comparable to that of MBE-grown films. In particular that the electrical behavior is consistent with the presence of a skyrmion state in the expected temperature and applied magnetic field range.

- Deposition of cubic FeGe by sputtering onto an MnSi film, this is the first bilayer of skyrmion-hosting materials.

- A new analytical approximation for single skyrmions which requires no undetermined fitting parameter and uses only physical conditions and properties to give a close match to time-consuming numerical calculations in the range of physical interest.

- Development of an analytical means to obtain an energy of the skyrmion (or combinations thereof) from this approximation.

- An extension of the approximation described above which appears to bridge the gap between the descriptions of isolated skyrmions against a uniform background and skyrmions as an intersection of three extended magnetization helices, each of which is very successful in its domain of applicability.

8.2 Future Directions

For the future there are a few important matters to take up. The final confirmation of the presence of skyrmions in the sputter-deposited films would be by Lorentz TEM, x-ray magnetic circular dichroism, or perhaps scanning probe techniques as they develop. Studying the transport properties of FeGe on MnSi in the regime where both can host skyrmions (of different sizes, 18nm for MnSi and 70nm for FeGe) should be interesting from the point of view of studying vertical interactions between the nominally two-dimensional skyrmions. Also, thinner films of MnSi should be deposited on Ta and the latter used to inject spin Hall currents in order to manipulate the skyrmions. This has been done for thin "normal" ferromagnets such as CoFeB but not for a chiral magnetic material like MnSi.

The approximation described in this thesis could be immediately applied to estimating skyrmion stability under different conditions in different materials and to studying

skyrmion dynamics. The most immediate problems to approach, beyond stability, are interactions between skyrmions including when they are close enough to each other that a rigid particle model for them is no longer appropriate, and the interaction of a skyrmion with a defect or barrier.

Appendices

A Appendix A: Numerical Procedure

Numerical solutions of Eq. (2.31) against which to compare the approximations of Chapter 7 are obtained using a shooting method calculation in the software package Mathematica. An important consideration for problems such as this with one boundary condition at infinity when solved by the shooting method is that a finite boundary point must be chosen and the boundary condition must be applied there. If the boundary point is too close to the origin then the numerical result will be invalid. It also introduces a level of approximation because in reality for the skyrmion profile problem, the profile decays to zero more slowly than any possible numerical approximation to the profile. When this problem is solved numerically in the literature [113], the boundary location is set when the solution obtained stops changing significantly.

The program defined below finds the most distant position for a boundary point at which the numerical solution is stable, thereby approximating a boundary condition at infinity. In addition, the condition for the stability of the solution is satisfied because boundary points chosen near the one found (but closer to the origin) give solutions for the profile function that are only infinitesimally different.

The first line is important because it allows Mathematica's own error handling rou-

tines to be used in determining whether a stable solution has been found and to continue the search if it has not. The expression at the end carries out the numerical solution procedure on the set of h,d values that was used to create the phenomenological parameters Eq. (7.11) for the approximation Eq. (7.10) with $x \to \rho$. Carrying out these calculations for the thirty-six values represented required five hours of computation on a standard desktop computer. The approximations presented in Chapter 7 are meant to save this time and allow rapid exploration of the physical parameter space.

```
1
2  Off[General::stop]
3
4  createLargestRegion[h_, d_, mult_] :=
5   Block[{bound = Min[mult*Abs[d]/h, 19], n = 1, result, previous},
6    While[Not[
7      Check[result[r_] :=
8       Evaluate[
9        First[\[Theta][r] /.
10         NDSolve[{\[Theta]''[r] + 1/r \[Theta]'[r] -
11             0.5/(r^2) Sin[2 \[Theta][r]] == (h /2 Sin[\[Theta][r]] +
12               d /r Sin[\[Theta][r]]^2 ), \[Theta][0.0001] ==
13            Pi, \[Theta][bound] == 0}, \[Theta][r], r,
14          "Method" -> {"Shooting",
15            " StartingInitialConditions " -> {\[Theta][.0001] ==
16               Pi, \[Theta]'[0.0001] == -Pi/1000}}]], False]] ||
17     FindMaximum[{result[t], t > .0001 && t <= bound}, t] > Pi ||
18     result [0.5] > result [0.0001],
19     bound = bound - 0.1;
20     n++;];
21     result[r]]
22
23 hdInterpFuncs =
```

```
Table[Table[{i*0.1, j*-0.1,
   Evaluate[createLargestRegion[i*0.1, j*-0.1, 19.0]]}, {j, 3, 18,
   3}], {i, 3, 18, 3}]
```

“newlabelA8528

B Appendix B: Energy Terms

“newlabelB85

```
FirstTerm = (a (a^2 Arg[1 + (-I + a Tanh[(b r)/2])/Sqrt[-1 + a^2]] -
     a^2 Arg[1 + (I + a Tanh[(b r)/2])/Sqrt[-1 + a^2]] -
     2 a^2 Sqrt[-1 + a^2] Cosh[b r] +
     Arg[1 + (-I + a Tanh[(b r)/2])/Sqrt[-1 + a^2]] Sinh[b r]^2 -
     Arg[1 + (I + a Tanh[(b r)/2])/Sqrt[-1 + a^2]] Sinh[b r]^2 +
     Arg[1 + (-I - a Tanh[(b r)/2])/Sqrt[-1 + a^2]] (a^2 +
        Sinh[b r]^2) -
     Arg[1 + (I - a Tanh[(b r)/2])/Sqrt[-1 + a^2]] (a^2 +
        Sinh[b r]^2)))/((-1 + a) (1 + a) Sqrt[-1 + a^2]
    b (a^2 + Sinh[b r]^2))

ThirdTermA=-1/(2 Sqrt[-a^2] b)
  a d (RootSum[1 - 2 #1^2 + 4 a^2 #1^2 + #1^4 &,
     1/(1 - #1^2 + 2 a^2 #1^2) (-b r Log[1 - E^(b r) #1] -
        PolyLog[2, E^(b r) #1] +
        Sqrt[-a^2] b r Log[1 - E^(b r) #1] #1 +
        Sqrt[-a^2] PolyLog[2, E^(b r) #1] #1 +
        b r Log[1 - E^(b r) #1] #1^2 -
        2 a^2 b r Log[1 - E^(b r) #1] #1^2 +
        PolyLog[2, E^(b r) #1] #1^2 -
        2 a^2 PolyLog[2, E^(b r) #1] #1^2 +
```

```
22          Sqrt[−a^2] b r Log[1 − E^(b r) #1] #1^3 +
23          Sqrt[−a^2] PolyLog[2, E^(b r) #1] #1^3) &] +
24      RootSum[1 − 2 #1^2 + 4 a^2 #1^2 + #1^4 &,
25       1/(1 − #1^2 + 2 a^2 #1^2) (b r Log[1 − E^(b r) #1] +
26          PolyLog[2, E^(b r) #1] +
27          Sqrt[−a^2] b r Log[1 − E^(b r) #1] #1 +
28          Sqrt[−a^2] PolyLog[2, E^(b r) #1] #1 −
29          b r Log[1 − E^(b r) #1] #1^2 +
30          2 a^2 b r Log[1 − E^(b r) #1] #1^2 −
31          PolyLog[2, E^(b r) #1] #1^2 +
32          2 a^2 PolyLog[2, E^(b r) #1] #1^2 +
33          Sqrt[−a^2] b r Log[1 − E^(b r) #1] #1^3 +
34          Sqrt[−a^2] PolyLog[2, E^(b r) #1] #1^3) &])
35
36 ThirdTermB=−((d R \[Delta] ArcTanh[Cosh[\[Rho]/\[Delta]]/Sqrt[1 − R^2]])/Sqrt[
37  1 − R^2])
38
39 FourthTerm = 1/(8 Sqrt[
40   a^2 (−1 + a^2)]) (−r Log[
41       1 − E^r/Sqrt[1 − 2 a^2 − 2 Sqrt[a^2 (−1 + a^2)]]] −
42    r Log[1 + E^r/Sqrt[1 − 2 a^2 − 2 Sqrt[a^2 (−1 + a^2)]]] +
43    r Log[1 − E^r/Sqrt[1 − 2 a^2 + 2 Sqrt[a^2 (−1 + a^2)]]] +
44    r Log[1 + E^r/Sqrt[1 − 2 a^2 + 2 Sqrt[a^2 (−1 + a^2)]]] −
45    PolyLog[2, −(E^r/Sqrt[1 − 2 a^2 − 2 Sqrt[a^2 (−1 + a^2)]])] −
46    PolyLog[2, E^r/Sqrt[1 − 2 a^2 − 2 Sqrt[a^2 (−1 + a^2)]]] +
47    PolyLog[2, −(E^r/Sqrt[1 − 2 a^2 + 2 Sqrt[a^2 (−1 + a^2)]])] +
48    PolyLog[2, E^r/Sqrt[1 − 2 a^2 + 2 Sqrt[a^2 (−1 + a^2)]]])
```

“newlabelB8652

Bibliography

[1] D. Frank, "Power-constrained CMOS scaling limits," *IBM Journal of Resarch and Development*, vol. 46, pp. 235–244, 2002.

[2] S. Deleonibus, "Physical and technological limitations of NanoCMOS devices to the end of the roadmap and beyond," *The European Physical Journal: Applied Physics*, vol. 36, pp. 197–214, 2007.

[3] D. Nikonov and I. Young, "Overview of beyond-cmos devices and a uniform methodology for their benchmarking," *Proceedings of the IEEE*, vol. 101, pp. 2498–2533, 2013.

[4] S. Parkin, "Shiftable magnetic shift register and method of using the same," 2004.

[5] S. Parkin, M. Hayashi, and L. Thomas, "Magnetic domain-wall racetrack memory," *Science*, vol. 320, p. 190, 2008.

[6] S. Parkin, "Data in the fast lanes of racetrack memory," *Scientific American*, vol. 300, pp. 76–81, June 2009.

[7] Everspin Technologies, Inc., "Spin-torque mram technical brief," 2013.

[8] J. Hayakawa, S. Ikeda, Y. Lee, R. Sasaki, T. Meguro, F. Matsukura, H. Takahashi, and H. Ohno, "Current-driven magnetization switching in CoFeB/MgO/CoFeB magnetic tunnel junctions," *Japanese Journal of Applied Physics*, vol. 44, pp. L1267–L1270, 2005.

[9] A. Fert, V. Cros, and J. Sampaio, "Skyrmions on the track," *Nature Nanotechnology*, vol. 8, pp. 152–156, 2013.

[10] N. Kiselev, A. Bogdanov, R. Schäfer, and U. Rößler, "Chiral skyrmions in thin magnetic films: new objects for magnetic storage technologies?," *Journal of Physics D: Applied Physics*, vol. 44, p. 392001, 2011.

[11] A. Bogdanov and D. Yablonskii, "Thermodynamically stable "vortices" in magnetically ordered crystals. the mixed state of magnets," *Soviet Physics JETP*, vol. 68, pp. 101–103, 1989.

[12] S. Mühlbauer, B. Binz, F. Jonietz, C. Pfleiderer, A. Rosch, A. Neubauer, R. Georgii, and P. Bni, "Skyrmion lattice in a chiral magnet," *Science*, vol. 323, no. 5916, pp. 915–919, 2009.

[13] T. Skyrme, "A unified field theory of mesons and baryons," *Nuclear Physics*, vol. 31, pp. 556–569, 1962.

[14] F. Rybakov, A. Borizov, and A. Bogdanov, "Three-dimensional skyrmion states in thin films of cubic helimagnets," *Physical Review B*, vol. 87, p. 094424, 2013.

[15] X. Z. Yu, Y. Onose, N. Kanazawa, J. H. Park, J. H. Han, Y. Matsui, N. Nagaosa, and Y. Tokura, "Real-space observation of a two-dimensional skyrmion crystal," *Nature*, vol. 465, pp. 901–904, Jun 2010.

[16] S.-Z. Lin, C. Reichhardt, C. D. Batista, and A. Saxena, "Particle model for skyrmions in metallic chiral magnets: Dynamics, pinning, and creep," *Phys. Rev. B*, vol. 87, p. 214419, Jun 2013.

[17] X. Yu, N. Kanazawa, W. Zhang, T. Nagai, T. Hara, K. Kimoto, Y. Matsui, Y. Onose, and Y. Tokura, "Skyrmion flow near room temperature in an ultralow current density," *Nature Communications*, vol. 3, p. 988, 2012.

[18] T. Yokouchi, N. Kanazawa, A. Tsukazaki, Y. Kozuka, A. Kikkawa, Y. Taguchi, M. Kawasaki, M. Ichikawa, F. Kagawa, and Y. Tokura, "Formation of in-plane skyrmions in epitaxial MnSi thin films as revealed by planar Hall effect," *Journal of the Physical Society of Japan*, vol. 84, no. 10, p. 104708, 2015.

[19] C. Schütte, J. Iwasaki, A. Rosch, and N. Nagaosa, "Inertia, diffusion, and dynamics of a driven skyrmion," *Phys. Rev. B*, vol. 90, p. 174434, Nov 2014.

[20] F. Buttner, C. Moutafis, M. Schneider, B. Kruger, C. M. Gunther, J. Geilhufe, C. v. K. Schmising, J. Mohanty, B. Pfau, S. Schaffert, A. Bisig, M. Foerster, T. Schulz, C. A. F. Vaz, J. H. Franken, H. J. M. Swagten, M. Klaui, and S. Eisebitt, "Dynamics and inertia of skyrmionic spin structures," *Nat Phys*, vol. 11, pp. 225–228, Mar 2015. Letter.

[21] T. Schulz, R. Ritz, A. Bauer, M. Halder, M. Wagner, C. Franz, C. Pfleiderer, K. Everschor, M. Garst, and A. Rosch, "Emergent electrodynamics of skyrmions in a chiral magnet," *Nat Phys*, vol. 8, pp. 301–304, Apr 2012.

[22] K. Hamamoto, M. Ezawa, and N. Nagaosa, "Quantized topological Hall effect in skyrmion crystal," *Phys. Rev. B*, vol. 92, p. 115417, Sep 2015.

[23] C.-Z. Chang, J. Zhang, X. Feng, J. Shen, Z. Zhang, M. Guo, K. Li, Y. Ou, P. Wei, L.-L. Wang, Z.-Q. Ji, Y. Feng, S. Ji, X. Chen, J. Jia, X. Dai, Z. Fang, S.-C. Zhang, K. He, Y. Wang, L. Lu, X.-C. Ma, and Q.-K. Xue, "Experimental observation of the quantum anomalous Hall effect in a magnetic topological insulator," *Science*, vol. 340, no. 6129, pp. 167–170, 2013.

[24] X. Kou, S.-T. Guo, Y. Fan, L. Pan, M. Lang, Y. Jiang, Q. Shao, T. Nie, K. Murata, J. Tang, Y. Wang, L. He, T.-K. Lee, W.-L. Lee, and K. L. Wang, "Scale-invariant quantum anomalous Hall effect in magnetic topological insulators beyond the two-dimensional limit," *Phys. Rev. Lett.*, vol. 113, p. 137201, Sep 2014.

[25] A. Schmeller, J. P. Eisenstein, L. N. Pfeiffer, and K. W. West, "Evidence for skyrmions and single spin flips in the integer quantized Hall effect," *Phys. Rev. Lett.*, vol. 75, pp. 4290–4293, Dec 1995.

[26] X. Zhang, G. P. Zhao, H. Fangohr, J. P. Liu, W. X. Xia, J. Xia, and F. J. Morvan, "Skyrmion-skyrmion and skyrmion-edge repulsions in skyrmion-based racetrack memory," *Scientific Reports*, vol. 5, pp. 7643 EP –, Jan 2015. Article.

[27] R. Rajaraman, *Solitons and Instantons*. North-Holland, 1989.

[28] T. Dauxois and M. Peyard, *Physics of Solitons*. Cambridge University Press, 2006.

[29] W. J. Zakrzewski, *Low Dimensional Sigma Models*. Adam Hilger, 1989.

[30] V. T. Dolgopolov, "Integer quantum Hall effect and related phenomena," *Physics-Uspekhi*, vol. 57, no. 2, p. 105, 2014.

[31] S. L. Sondhi, A. Karlhede, S. A. Kivelson, and E. H. Rezayi, "Skyrmions and the crossover from the integer to fractional quantum Hall effect at small Zeeman energies," *Phys. Rev. B*, vol. 47, pp. 16419–16426, Jun 1993.

[32] H. A. Fertig, L. Brey, R. Côté, A. H. MacDonald, A. Karlhede, and S. L. Sondhi, "Hartree-Fock theory of skyrmions in quantum Hall ferromagnets," *Phys. Rev. B*, vol. 55, pp. 10671–10680, Apr 1997.

[33] F. Freimuth, R. Bamler, Y. Mokrousov, and A. Rosch, "Phase-space Berry phases in chiral magnets: Dzyaloshinskii-Moriya interaction and the charge of skyrmions," *Phys. Rev. B*, vol. 88, p. 214409, Dec 2013.

[34] A. A. Belain and A. Polyakov, "Metastable states of two-dimensional isotropic ferromagnets," *JETP Letters*, vol. 22, no. 10, p. 245, 1975.

[35] A. Bogdanov and A. Hubert, "Thermodynamically stable magnetic vortex states in magnetic crystals," *Journal of Magnetism and Magnetic Materials*, vol. 138, no. 3, pp. 255 – 269, 1994.

[36] M. V. Berry, "Quantal phase factors accompanying adiabatic changes," *Proceedings of the Royal Society of London A: Mathematical, Physical and Engineering Sciences*, vol. 392, no. 1802, pp. 45–57, 1984.

[37] A. Bohm, A. Mostafazadeh, H. Koizumi, Q. Niu, and J. Zwanziger, *The Geometric Phase in Quantum systems*. Springer, 2003.

[38] D. Chruscinski and A. Jamiolkowski, *Geometric Phases in Classical and Quantum Mechanics*. Birkhauser, 2004.

[39] B. Simon, "Holonomy, the quantum adiabatic theorem, and Berry's phase," *Phys. Rev. Lett.*, vol. 51, pp. 2167–2170, Dec 1983.

[40] J. W. Zwanziger, M. Koenig, and A. Pines, "Berry's phase," *Annual Review of Physical Chemistry*, vol. 41, no. 1, pp. 601–646, 1990.

[41] S. Tomonaga, *The Story of Spin*. University of Chicago Press, 1998.

[42] J. D. Jackson, *Classical Electrodynamics*. Wiley, 3rd ed., 1999.

[43] L. H. Thomas, "Motion of the spinning electron," *Nature*, vol. 117, p. 514, 1926.

[44] H. Goldstein, C. P. Poole, and J. L. Safko, *Classical Mechanics (3rd Edition)*. Addison-Wesley, 2001.

[45] L. Thomas, "The kinematics of an electron with an axis," *The London, Edinburgh, and Dublin Philosophical Magazine and Journal of Science*, vol. 3, no. 13, pp. 1–22, 1927.

[46] E. Wigner, "On unitary representations of the inhomogeneous Lorentz group," *Annals of Mathematics*, vol. 40, no. 1, pp. pp. 149–204, 1939.

[47] D. Xiao, M.-C. Chang, and Q. Niu, "Berry phase effects on electronic properties," *Rev. Mod. Phys.*, vol. 82, pp. 1959–2007, Jul 2010.

[48] J. Zak, "Berry's phase for energy bands in solids," *Phys. Rev. Lett.*, vol. 62, pp. 2747–2750, Jun 1989.

[49] Y. Mokrousov and F. Freimuth, "Geometric Phases and Topological Effects," *ArXiv e-prints*, July 2014.

[50] N. Nagaosa, "Anomalous Hall effect a new perspective," *Journal of the Physical Society of Japan*, vol. 75, no. 4, p. 042001, 2006.

[51] G. Y. Guo, S. Murakami, T.-W. Chen, and N. Nagaosa, "Intrinsic spin Hall effect in platinum: First-principles calculations," *Phys. Rev. Lett.*, vol. 100, p. 096401, Mar 2008.

[52] G. Y. Guo, Y. Yao, and Q. Niu, "*Ab initio* calculation of the intrinsic spin Hall effect in semiconductors," *Phys. Rev. Lett.*, vol. 94, p. 226601, Jun 2005.

[53] I. Dzyaloshinskii, "A thermodynamic theory of "weak" ferromagnetism of antiferromagnetics," *Journal of Physics and Chemistry of Solids*, vol. 4, pp. 241–255, 1958.

[54] T. Moriya, "Anisotropic superexchange interaction and weak ferromagnetism," *Physical Review*, vol. 120, pp. 91–98, 1960.

[55] F. Freimuth, S. Blügel, and Y. Mokrousov, "Berry phase theory of Dzyaloshinskii Moriya interaction and spinorbit torques," *Journal of Physics: Condensed Matter*, vol. 26, no. 10, p. 104202, 2014.

[56] U. K. Rößler, A. A. Leonov, and A. N. Bogdanov, "Chiral skyrmionic matter in non-centrosymmetric magnets," *Journal of Physics: Conference Series*, vol. 303, no. 1, p. 012105, 2011.

[57] N. Manton and P. Sutcliffe, *Topological Solitons*. Cambridge University Press, 2004.

[58] R. A. Leese, M. Peyrard, and W. J. Zakrzewski, "Soliton stability in the o(3) sigma -model in (2+1) dimensions," *Nonlinearity*, vol. 3, no. 2, p. 387, 1990.

[59] T. Ioannidou, V. Kopeliovich, and W. Zakrzewski, "Approximate analytical solutions of the baby skyrme model," *Journal of Experimental and Theoretical Physics*, vol. 95, no. 3, pp. 572–580, 2002.

[60] A. Kosevich, B. Ivanov, and A. Kovalev, "Magnetic solitons," *Physics Reports*, vol. 194, no. 34, pp. 117 – 238, 1990.

[61] P. Milde, Köhler, J. Seidel, L. Eng, A. Bauer, A. Chacon, J. Kindervater, S. Mühlbauer, C. Pfleiderer, S. Buhrandt, C. Schütte, and A. Rosch, "Unwinding of a skyrmion lattice by magnetic monopoles," *Science*, vol. 340, pp. 1076–1080, 2013.

[62] M. Pelliccione, A. Jenkins, P. Ovartchaiyapong, C. Reetz, E. Emmanuelidu, N. Ni, and A. C. Bleszynski Jayich, "Scanned probe imaging of nanoscale magnetism at cryogenic temperatures with a single-spin quantum sensor," *ArXiv e-prints*, Oct. 2015.

[63] N. Romming, C. Hanneken, M. Menzel, J. Bickel, B. Wolter, K. von Bergmann, A. Kubetzka, and R. Wiesendanger, "Writing and deleting single magnetic skyrmions," *Science*, vol. 341, pp. 636–639, 2013.

[64] A. Petford-Long and M. DeGraef, *Lorentz Microscopy*. Wiley, 2003.

[65] Y. Li, N. Kanazawa, X. Z. Yu, A. Tsukazaki, M. Kawasaki, M. Ichikawa, X. F. Jin, F. Kagawa, and Y. Tokura, "Robust formation of skyrmions and topological Hall effect anomaly in epitaxial thin films of MnSi," *Phys. Rev. Lett.*, vol. 110, p. 117202, Mar 2013.

[66] Y. X.Z., J. DeGrave, Y. Hara, T. Hara, S. Jin, and Y. Tokura, "Observation of the magnetic skyrmion lattice in a MnSi nanowire by Lorentz TEM," *Nano Letters*, vol. 13, pp. 3755–3759, 2013.

[67] M. Nagao, Y.-G. So, H. Yoshida, K. Yamaura, T. Nagai, T. Hara, A. Yamazaki, and K. Kimoto, "Experimental observation of multiple-q states for the magnetic skyrmion lattice and skyrmion excitations under a zero magnetic field," *Phys. Rev. B*, vol. 92, p. 140415, Oct 2015.

[68] T. L. Monchesky, J. C. Loudon, M. D. Robertson, and A. N. Bogdanov, "Comment on "robust formation of skyrmions and topological Hall effect anomaly in epitaxial thin films of MnSi"," *Phys. Rev. Lett.*, vol. 112, p. 059701, Feb 2014.

[69] M. N. Wilson, A. B. Butenko, A. N. Bogdanov, and T. L. Monchesky, "Chiral skyrmions in cubic helimagnet films: The role of uniaxial anisotropy," *Phys. Rev. B*, vol. 89, p. 094411, Mar 2014.

[70] S. A. Meynell, M. N. Wilson, J. C. Loudon, A. Spitzig, F. N. Rybakov, M. B. Johnson, and T. L. Monchesky, "Hall effect and transmission electron microscopy of epitaxial MnSi thin films," *Phys. Rev. B*, vol. 90, p. 224419, Dec 2014.

[71] A. Neubauer, C. Pfleiderer, B. Binz, A. Rosch, R. Ritz, P. G. Niklowitz, and P. Böni, "Topological Hall effect in the *a* phase of MnSi," *Phys. Rev. Lett.*, vol. 102, p. 186602, May 2009.

[72] M. Lee, Y. Onose, Y. Tokura, and N. P. Ong, "Hidden constant in the anomalous Hall effect of high-purity magnet MnSi," *Phys. Rev. B*, vol. 75, p. 172403, May 2007.

[73] N. Kanazawa, M. Kubota, A. Tsukazaki, Y. Kozuka, K. S. Takahashi, M. Kawasaki, M. Ichikawa, F. Kagawa, and Y. Tokura, "Discretized topological Hall effect emerging from skyrmions in constricted geometry," *Phys. Rev. B*, vol. 91, p. 041122, Jan 2015.

[74] S. D. Yi, S. Onoda, N. Nagaosa, and J. H. Han, "Skyrmions and anomalous Hall effect in a Dzyaloshinskii-Moriya spiral magnet," *Phys. Rev. B*, vol. 80, p. 054416, Aug 2009.

[75] B. Chapman, M. Grossnickle, T. Wolf, and M. Lee, "Large enhancement of emergent magnetic fields in MnSi with impurities and pressure," *Physical Review B*, vol. 88, p. 214406, 2013.

[76] A. Neubauer, C. Pfleiderer, R. Ritz, P. Niklowitz, and P. Bni, "Hall effect and magnetoresistance in MnSi," *Physica B: Condensed Matter*, vol. 404, no. 19, pp. 3163 – 3166, 2009. Proceedings of the International Conference on Strongly Correlated Electron Systems.

[77] J. M. Higgins, R. Ding, J. P. DeGrave, and S. Jin, "Signature of helimagnetic ordering in single-crystal MnSi nanowires," *Nano Letters*, vol. 10, no. 5, pp. 1605–1610, 2010. PMID: 20387800.

[78] S. V. Demishev, I. I. Lobanova, N. E. Sluchanko, and V. V. Glushkov, "Macroscopic evidence of skyrmion lattice inhomogeneity and magnetic vortex states in the A-phase of MnSi," *ArXiv e-prints*, July 2015.

[79] Y. Tokunaga, X. Z. Yu, J. S. White, H. M. Ronnow, D. Morikawa, Y. Taguchi, and Y. Tokura, "A new class of chiral materials hosting magnetic skyrmions beyond room temperature," *Nat Commun*, vol. 6, Jul 2015.

[80] S. Woo, K. Litzius, B. Krüger, M.-Y. Im, L. Caretta, K. Richter, M. Mann, A. Krone, R. Reeve, M. Weigand, P. Agrawal, P. Fischer, M. Kläui, and G. S. D. Beach, "Observation of room temperature magnetic skyrmions and their current-driven dynamics in ultrathin Co films," *ArXiv e-prints*, Feb. 2015.

[81] A. Abrikosov, "The magnetic properties of superconducting alloys," *Journal of Physics and Chemistry of Solids*, vol. 2, no. 3, pp. 199 – 208, 1957.

[82] F. Chen, *Introduction to Plasma Physics*. Springer, 1974.

[83] S. X. Huang and C. L. Chien, "Extended skyrmion phase in epitaxial FeGe(111) thin films," *Phys. Rev. Lett.*, vol. 108, p. 267201, Jun 2012.

[84] L. Landau and E. Lifshitz, *Electrodynamics of Continuous Media*. Pergamon, 1960.

[85] N. Ashcroft and N. Mermin, *Solid State Physics*. Holt, Rinehart and Winston, 1977.

[86] B. He, *Two-Dimensional X-Ray Diffraction*. Wiley, 2009.

[87] T. J. Sato, "In-plane skyrmion strings now observed in epitaxial thin films," *JPSJ News and Comments*, vol. 12, p. 10, 2015.

[88] J. Sinova, S. O. Valenzuela, J. Wunderlich, C. H. Back, and T. Jungwirth, "Spin Hall effects," *Rev. Mod. Phys.*, vol. 87, pp. 1213–1260, Oct 2015.

[89] S. Takahashi and S. Maekawa, "Spin current, spin accumulation and spin Hall effect," *Science and Technology of Advanced Materials*, vol. 9, no. 1, p. 014105, 2008.

[90] L. Liu, C.-F. Pai, Y. Li, H. W. Tseng, D. C. Ralph, and R. A. Buhrman, "Spin-torque switching with the giant spin Hall effect of tantalum," *Science*, vol. 336, no. 6081, pp. 555–558, 2012.

[91] K. Kadowaki, K. Okuda, and M. Date, "Magnetization and magnetoresistance of MnSi. I," *Journal of the Physical Society of Japan*, vol. 51, no. 8, pp. 2433–2438, 1982.

[92] S. V. Demishev, V. V. Glushkov, I. I. Lobanova, M. A. Anisimov, V. Y. Ivanov, T. V. Ishchenko, M. S. Karasev, N. A. Samarin, N. E. Sluchanko, V. M. Zimin, and A. V. Semeno, "Magnetic phase diagram of MnSi in the high-field region," *Phys. Rev. B*, vol. 85, p. 045131, Jan 2012.

[93] P. Schilbe and K. H. Rieder, "Possible determination of critical exponents from experimental magnetization data of ferromagnetic thin films," *EPL (Europhysics Letters)*, vol. 41, no. 2, p. 219, 1998.

[94] Q. Hong, "Critical temperature of an Ising magnetic film," *Phys. Rev. B*, vol. 41, pp. 9621–9624, May 1990.

[95] Y. Laosiritaworn, J. Poulter, and J. B. Staunton, "Magnetic properties of Ising thin films with cubic lattices," *Phys. Rev. B*, vol. 70, p. 104413, Sep 2004.

[96] J. Geicke, "An approach to radially symmetrical solutions of the sine-Gordon equation," *Physica D: Nonlinear Phenomena*, vol. 4, no. 2, pp. 197 – 206, 1982.

[97] A. Saxena and R. Dandoloff, "Heisenberg spins on a cylinder in an axial magnetic field," *Phys. Rev. B*, vol. 58, pp. R563–R566, Jul 1998.

[98] J. Rubinstein, "SineGordon equation," *Journal of Mathematical Physics*, vol. 11, no. 1, 1970.

[99] A. Barone, F. Esposito, C. Magee, and A. Scott, "Theory and applications of the sine-Gordon equation," *La Rivista del Nuovo Cimento (1971-1977)*, vol. 1, no. 2, pp. 227–267, 1971.

[100] L. D. Landau and E. Lifshitz, "On the theory of the dispersion of magnetic permeability in ferromagnetic bodies," *Physik. Zeits. Sowjetunion*, vol. 8, p. 153, 1935.

[101] H. J. Mikeska, "Solitons in a one-dimensional magnet with an easy plane," *Journal of Physics C: Solid State Physics*, vol. 11, no. 1, p. L29, 1978.

[102] H. J. Mikeska, "Solitons in one-dimensional magnets (invited)," *Journal of Applied Physics*, vol. 52, no. 3, 1981.

[103] U. Enz, "Die dynamik der bloschen wand," *Helvetica Physica Acta*, vol. 37, no. 3, p. 1325, 1964.

[104] A. R. Bishop and W. F. Lewis, "A theory of intrinsic coercivity in narrow magnetic domain wall materials," *Journal of Physics C: Solid State Physics*, vol. 12, no. 18, p. 3811, 1979.

[105] R. Wieser, E. Y. Vedmedenko, and R. Wiesendanger, "Domain wall motion damped by the emission of spin waves," *Phys. Rev. B*, vol. 81, p. 024405, Jan 2010.

[106] J. Perring and T. Skyrme, "A model unified field equation," *Nuclear Physics*, vol. 31, pp. 550 – 555, 1962.

[107] P. M. Sutcliffe, "Skyrmions from kinks," *Physics Letters B*, vol. 292, no. 12, pp. 104 – 106, 1992.

[108] M. Nitta, "Josephson vortices and the Atiyah-Manton construction," *Phys. Rev. D*, vol. 86, p. 125004, Dec 2012.

[109] K. A. Long and A. R. Bishop, "Nonlinear excitations in classical ferromagnetic chains," *Journal of Physics A: Mathematical and General*, vol. 12, no. 8, p. 1325, 1979.

[110] M. Lakshmanan, T. Ruijgrok, and C. Thompson, "On the dynamics of a continuum spin system," *Physica A: Statistical Mechanics and its Applications*, vol. 84, no. 3, pp. 577 – 590, 1976.

[111] H.-B. Braun, "Fluctuations and instabilities of ferromagnetic domain-wall pairs in an external magnetic field," *Phys. Rev. B*, vol. 50, pp. 16485–16500, Dec 1994.

[112] P. V. Paulau, D. Gomila, P. Colet, B. A. Malomed, and W. J. Firth, "From one- to two-dimensional solitons in the Ginzburg-Landau model of lasers with frequency-selective feedback," *Phys. Rev. E*, vol. 84, p. 036213, Sep 2011.

[113] A. Bogdanov and A. Hubert, "The stability of vortex-like structures in uniaxial ferromagnets," *Journal of Magnetism and Magnetic Materials*, vol. 195, no. 1, pp. 182 – 192, 1999.